

PEARLS: NuSTAR and XMM-Newton Extragalactic Survey of the JWST North Ecliptic Pole Time-Domain Field II

XIURUI ZHAO ¹, FRANCESCA CIVANO ², CHRISTOPHER N. A. WILLMER ³, SILVIA BONOLI ^{4,5},
CHIEN-TING CHEN ^{6,7}, SAMANTHA CREECH ⁸, RENATO DUPKE ^{9,10,11}, FRANCESCA M. FORNASINI ¹²,
ROLF A. JANSEN ¹³, SATOSHI KIKUTA ¹⁴, ANTON M. KOEKEMOER ¹⁵, SIBASISH LAHA ^{16,2},
STEFANO MARCHESI ^{17,18,19}, ROSALIA O'BRIEN ⁹, ROSS SILVER ², S. P. WILLNER ¹, ROGIER A. WINDHORST ¹³,
HAOJING YAN ²¹, JAILSON ALCANIZ ⁹, NARCISO BENITEZ ²², SAULO CARNEIRO ²², JAVIER CENARRO ²³,
DAVID CRISTÓBAL-HORNILLOS ²³, ALESSANDRO EDEROCLITE ²³, ANTONIO HERNÁN-CABALLERO ²³,
CARLOS LÓPEZ-SANJUAN ²³, ANTONIO MARÍN-FRANCH ²³, CLAUDIA MENDES DE OLIVEIRA ²⁴, MARIANO MOLES ²³,
LAERTE SODRÉ JR. ²⁵, KEITH TAYLOR ²⁶, JESÚS VARELA ²³, AND HÉCTOR VÁZQUEZ RAMIÓ ²³

¹Center for Astrophysics | Harvard & Smithsonian, 60 Garden Street, Cambridge, MA 02138, USA

²NASA Goddard Space Flight Center, Greenbelt, MD 20771, USA

³Steward Observatory, University of Arizona, 933 North Cherry Avenue, Tucson, AZ 85721, USA

⁴Donostia International Physics Center (DIPC), Manuel Lardizabal Ibilbidea, 4, San Sebastian, Spain

⁵Ikerbasque, Basque Foundation for Science, E-48013 Bilbao, Spain

⁶Science and Technology Institute, Universities Space Research Association, Huntsville, AL 35805, USA

⁷Astrophysics Office, NASA Marshall Space Flight Center, ST12, Huntsville, AL 35812, USA

⁸Department of Physics & Astronomy, University of Utah, 115 South 1400 East, Salt Lake City, UT 84112, USA

⁹Observatório Nacional, Rua General José Cristino, 77, São Cristóvão, 20921-400, Rio de Janeiro, RJ, Brazil

¹⁰Department of Astronomy, University of Michigan, 311 West Hall, 1085 South University Ave., Ann Arbor, MI 48109, USA

¹¹Department of Physics and Astronomy, University of Alabama, Box 870324, Tuscaloosa, AL 35487-0324, USA

¹²Department of Physics and Astronomy, Stonehill College, 320 Washington Street, Easton, MA 02357, USA

¹³School of Earth and Space Exploration, Arizona State University, P.O. Box 871404, Tempe, AZ 85287-1404, USA

¹⁴National Astronomical Observatory of Japan, 2-21-1 Osawa, Mitaka, Tokyo 181-8588, Japan

¹⁵Space Telescope Science Institute, 3700 San Martin Drive, Baltimore, MD 21218, USA

¹⁶Center for Space Science and Technology, University of Maryland Baltimore County, 1000 Hilltop Circle, Baltimore, MD 21250, USA

¹⁷Dipartimento di Fisica e Astronomia (DIFA), Università di Bologna, via Gobetti 93/2, I-40129 Bologna, Italy

¹⁸Department of Physics and Astronomy, Clemson University, Kinard Lab of Physics, Clemson, SC 29634, USA

¹⁹INAF, Osservatorio di Astrofisica e Scienza dello Spazio di Bologna, via P. Gobetti 93/3, 40129 Bologna, Italy

²⁰School of Earth and Space Exploration, Arizona State University, Tempe, AZ 85287-1404, USA

²¹Department of Physics and Astronomy, University of Missouri, Columbia, MO 65211, USA

²²Instituto de Física, Universidade Federal da Bahia, 40210-340, Salvador, BA, Brazil

²³Centro de Estudios de Física del Cosmos de Aragón (CEFCA), Plaza San Juan, 1, E-44001, Teruel, Spain

²⁴Departamento de Astronomia, Instituto de Astronomia, Geofísica e Ciências Atmosféricas, Universidade de São Paulo, São Paulo, Brazil

²⁵IAG/USP - Departamento de Astronomia, Instituto de Astronomia, Geofísica e Ciências Atmosféricas, Universidade de São Paulo, São Paulo, Brazil

²⁶Instruments4, 4121 Pembury Place, La Canada Flintridge, CA 91011, U.S.A.

ABSTRACT

We present the second NuSTAR and XMM-Newton extragalactic survey of the JWST North Ecliptic Pole (NEP) Time-Domain Field (TDF). The first NuSTAR NEP-TDF survey (Zhao et al. 2021) had 681 ks total exposure time executed in NuSTAR cycle 5, in 2019 and 2020. This second survey, acquired from 2020 to 2022 in cycle 6, adds 880 ks of NuSTAR exposure time. The overall NuSTAR NEP-TDF survey is the most sensitive NuSTAR extragalactic survey to date, and a total of 60 sources were detected above the 95% reliability threshold. We constrain the hard X-ray number counts, $\log N - \log S$, down to 1.7×10^{-14} erg cm⁻² s⁻¹ at 8–24 keV and detect an excess of hard X-ray sources at the faint end. About 47% of the NuSTAR-detected sources are heavily obscured ($N_{\text{H}} > 10^{23}$ cm⁻²), and $18^{+20}_{-8}\%$ of the NuSTAR-detected sources are Compton-thick ($N_{\text{H}} > 10^{24}$ cm⁻²). These fractions are consistent with those measured in other NuSTAR surveys. Four sources presented $>2\sigma$ variability in the 3-year survey. In addition to NuSTAR, a total of 62 ks of XMM-Newton observations were taken

during NuSTAR cycle 6. The XMM-Newton observations provide soft X-ray (0.5–10 keV) coverage in the same field and enable more robust identification of the visible and infrared counterparts of the NuSTAR-detected sources. A total of 286 soft X-ray sources were detected, out of which 214 XMM-Newton sources have secure counterparts from multiwavelength catalogs.

Keywords: X-ray surveys(1824), Active galactic nuclei(16)

1. INTRODUCTION

The Nuclear Spectroscopic Telescope Array (NuSTAR) mission, launched in June 2012, is the first telescope focusing hard X-rays (3–79 keV; [Harrison et al. 2013](#)). The 100 times deeper hard X-ray sensitivity of NuSTAR compared with the previous collimated or coded mask instruments allows the peak (20–40 keV) of the Cosmic X-ray background (CXB) to be resolved into individual objects. Indeed, about 35–60% of the CXB at 8–24 keV was resolved by previous NuSTAR extragalactic surveys (Hickox et al., in prep).

NuSTAR performed a series of extragalactic surveys in its first two-year baseline mission to probe AGN activity over cosmic time. The surveys followed a wedding cake strategy covering from small areas with deep exposures and broader surveys with shallow exposures (see, [Zhao et al. 2021a](#), hereafter Z21, for an overview).

JWST, successfully launched on Dec. 25, 2021, is a NASA/ESA/CSA Flagship mission focusing on near- and mid-infrared wavelengths (0.6–28.5 μm) with its 6.5 m aperture and state-of-the-art scientific instruments ([Gardner et al. 2006, 2023](#)). JWST Interdisciplinary Scientist (IDS) R. Windhorst allocated ~ 47 hours of his guaranteed time to the North Ecliptic Pole (NEP) time-domain field (TDF) is part of the “Prime Extragalactic Areas for Reionization and Lensing Science” (PEARLS) project (GTO-2738; [Windhorst et al. 2023](#)). JWST has observed this field in four orthogonal spikes in cycle 1. Each observation includes eight filters of NIRCам observations and coordinated parallel observations with NIRISS/WFSS. This field was selected to be located within the JWST northern continuous viewing zone (CVZ) to enable time-domain studies. Furthermore, this NEP-TDF has the best combination of low foreground extinction and absence of $AB \leq 16$ mag stars ([Jansen & Windhorst 2018](#)). The NEP-TDF has become a comprehensive multiwavelength survey.¹ The multiwavelength coverage of the NEP-TDF approved to date is presented in Table 1.

This paper presents the multi-year NuSTAR and XMM-Newton extragalactic survey in the NEP-TDF. The paper’s focus is the two X-ray source catalogs. The paper is organized as follows. Section 2 describes the NuSTAR data reduction. Section 3 describes the construction of simulated data and the resulting reliability, completeness, sensitivity, positional uncertainty, and input-measured relation of the NuSTAR NEP-TDF survey. Section 4 presents the NuSTAR source catalog. Section 5 describes our XMM-Newton source detection and astrometric corrections, the sensitivity, and the XMM-Newton catalog including matching with NuSTAR. Section 6 describes matching XMM-Newton sources to existing visible-wavelength and infrared (IR) catalogs using a maximum-likelihood method. We present the X-ray to optical properties of these sources. Section 7 discusses the number counts of the sources as a function of flux, the X-ray hardness ratios, and the Compton-thick (CT) fraction. The Appendixes present the source catalogs of both the NuSTAR and XMM-Newton NEP-TDF surveys, spectroscopic redshifts of some VLA and Chandra detected sources in the NEP-TDF, and a newly developed pipeline to analyze source variability of NuSTAR observations.

Uncertainties are quoted at a 90% confidence level throughout the paper unless otherwise stated. Magnitudes used here are in the AB system, and standard cosmological parameters are adopted as follows: $H_0 = 70 \text{ km s}^{-1} \text{ Mpc}^{-1}$, $\Omega_M = 0.30$, and $\Omega_\Lambda = 0.70$.

2. NuSTAR DATA PROCESSING

NuSTAR (3–24 keV) surveyed the NEP-TDF in both cycle 5 (PI: Civano, ID: 5192) and cycle 6 (PI: Civano, ID: 6218, two-year program). The cycle 5 results were published ([Z21](#)). This work focused on the cycle 6 and the combined cycles 5 and 6 data. The NuSTAR cycle 6 NEP-TDF survey comprises 12 observations taken in four epochs spanning from 2020 Oct. to 2022 Jan. with a total of 880 ks exposure time. The cycle 6 survey was designed with a primary focus on variability, and therefore each epoch’s observations pointed to the

¹ A comprehensive table can be found at <http://lambda.la.asu.edu/jwst/neptdf/>

Table 1. Approved NEP-TDF multiwavelength surveys.

Telescope	PI	Exposure	Reference
NuSTAR	F. Civano	3.3 Ms	Zhao et al. (2021a)
XMM-Newton	F. Civano	120 ks	Zhao et al. (2021a)
Chandra	W. P. Maksym	1.8 Ms	Maksym et al., in prep.
AstroSat/UVIT	K. Saha	98 hrs	
HST/WFC3+ACS	R. Jansen & N. Grogin	173 hrs	O'Brien et al. (2024) , Jansen et al., in prep.
LBT/LBC	R. Jansen	11 hrs	
Subaru/HSC	G. Hasinger & E. Hu	5 hrs	Taylor et al. (2023)
GTC/HiPERCAM	V. Dhillon	16 hrs	
TESS	G. Berriman & B. Holwerda	357 days	
MMT/MMIRS	C. N. A. Willmer	68 hrs	Willmer et al. (2023)
JWST/NIRCam+NIRISS	R. A. Windhorst & H. B. Hammel	49 hrs	Windhorst et al. (2023) ; Adams et al. (2023)
JCMT/SCUBA-2	I. Smail & M. Im	63 hrs	Hyun et al. (2023)
IRAM/NIKA 2	S. H. Cohen	30 hrs	
SMA	G. Fazio	112 hrs	
VLA	R. A. Windhorst & W. Cotton	47 hrs	Hyun et al. (2023) ; Willner et al. (2023)
VLBA	W. Brisken	137 hrs	
eMERLIN	A. Thomson	140 hrs	
LOFAR	R. Van Weeren	72 hrs	
Spectroscopic			
J-PAS (56 filters)	S. Bonoli & R. Dupke	29 hrs	Hernán-Caballero et al. (2023)
MMT/Binospec	C. N. A. Willmer	26 hrs	Willmer et al., in prep.
MMT/MMIRS	C. N. A. Willmer	11 hrs	Willmer et al., in prep.

same area with similar effective position angles.² Table 2 presents the details of the individual NuSTAR observations in cycle 5 and cycle 6. This work, following previous NuSTAR extragalactic surveys, focuses on the 3–24 keV band because only the brightest sources can be detected at >24 keV owing to the decrease of the effective area and significant increase of the background at >24 keV (e.g., [Masini et al. 2018a](#)).

2.1. Data Reduction

The reduction of the cycle 6 observations used the same method as for the cycle 5 data ([Z21](#)). In brief, the NuSTAR data were processed using HEASoft v.6.29c and NuSTAR Data Analysis Software (NuSTARDAS) v.2.1.1 with the updated calibration and response files CALDB v.20211115. The level 1 raw data were calibrated, cleaned, and screened by running the `nupipeline` tool. Following [Z21](#), we removed the high-background time intervals (when the count rate in the

3.5–9.5 keV band was at least double the average count rate of the entire observation) in each observation. The total exposure losses of the two NuSTAR focal plane modules (FPMs) due to the high background were 6.5 ks and 8 ks for FPMA and FPMB, respectively, corresponding to 0.8% of the entire cycle 6 NuSTAR NEP-TDF survey exposures.

2.2. Exposure Map Production

We generated the vignetting-corrected exposure map of each NuSTAR observation in three energy bands: 3–24 keV, 3–8 keV, and 8–24 keV using the NuSTARDAS tool `nuexpomap`. The exposure map of the entire cycle 6 survey was produced by merging the 12 individual maps into a mosaic. That included merging the two FPMs' observations as FPMA+B. Figure 1 shows the cumulative areas as a function of the vignetting-corrected exposure in the three energy bands. The cycle 6 survey repeatedly observed the same region, so its exposure is ~60% deeper than the cycle 5 survey (Figure 1) but with ~35% smaller area coverage (~0.107 deg² in cycle 6 compared with ~0.16 deg² in cycle 5). To achieve the deepest exposure, we also merged the cycle 5 and

² NuSTAR reaches similar effective position angles every 3 month due to its square CCD, but the source might lie on different sub-detectors in different epochs.

Table 2. List of NuSTAR and XMM-Newton observations.

ObsID	Date	R.A. (deg)	Dec. (deg)	Exp. (ks)
Cycle 5 NuSTAR				
60511001002	2019-09-30	260.8664	65.8298	73.5
60511002002	2019-10-02	260.7643	65.8305	77.6
60511003002	2019-10-04	260.6297	65.8316	68.7
60511004002	2020-01-03	260.4992	65.9184	89.8
60511005002	2020-01-04	260.7289	65.8757	84.7
60511006002	2020-01-05	260.8676	65.9159	83.0
60511007002	2020-03-01	260.5070	65.7602	65.2
60511008001	2020-03-02	260.7292	65.7406	70.2
60511009001	2020-03-03	260.9369	65.7399	68.3
Total				681
Cycle 6 NuSTAR				
60666001002	2020-10-18	260.8664	65.8298	72.8
60666002002	2020-10-13	260.6219	65.8075	71.9
60666003002	2020-10-15	260.8534	65.8463	72.7
60666004002	2021-01-14	260.6508	65.8776	76.9
60666005002	2021-01-17	260.6541	65.7791	77.5
60666006002	2021-01-18	260.8448	65.8204	80.4
60666007002	2021-10-12	260.5930	65.9025	78.1
60666008002	2021-10-14	260.5868	65.7996	49.9
60666009002	2021-10-15	260.8223	65.8393	52.7
60666010002	2022-01-19	260.6164	65.8882	80.9
60666011002	2022-01-22	260.5980	65.7878	82.9
60666012002	2022-01-23	260.8546	65.8173	82.9
Total				880
Cycle 6 XMM				
0870860101	2020-10-14	260.6917	65.8711	17.0
0870860201	2021-01-16	260.6917	65.8711	23.2
0870860301 ^a	2021-10-14	260.6917	65.8711	0*
0870860401	2022-01-24	260.6917	65.8711	21.9
Total				62

^aThis observation was entirely lost to high particle background during the observation.

cycle 6 observations to achieve a central exposure time of ≈ 1.7 Ms (FPMA+B). We used the 8–24 keV exposure map to present the 8–16 keV, and 16–24 keV exposure maps as they show only marginal differences.

2.3. Observation Mosaic Creation

For each of the 12 cycle 6 observations, summed FPMA+B mosaics were created in five energy bands:

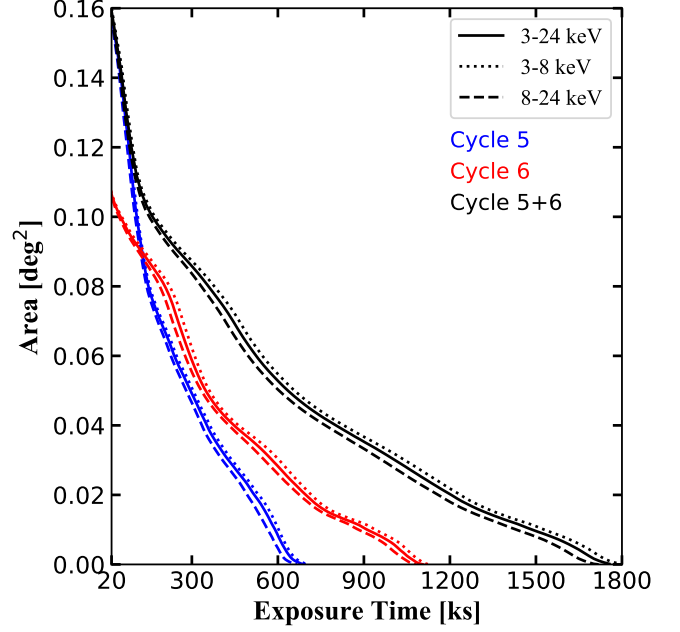


Figure 1. Cumulative survey area as a function of the FPMA+B vignetting-corrected exposure time. Colors distinguish the NuSTAR NEP-TDF surveys in cycle 5 (blue), cycle 6 (red), and combined cycles 5+6 (black), and line types distinguish energy bands as shown in the legend.

3–24 keV, 3–8 keV, 8–24 keV, 8–16 keV, and 16–24 keV. The five bands were separated using the `HEASoft Xselect` tool. Each band was then merged into a full-exposure mosaic using the `Ximage` tool. Loss of spatial resolution due to the resampling is negligible because the pixel angular resolution ($2''.45$) of the standard NuSTAR sky binning by NuSTARDAS is much smaller than the $\sim 18''$ full width at half-maximum (FWHM) of NuSTAR. The cycle 6 mosaic was also merged with the cycle 5 mosaic to achieve the deepest sensitivity. The astrometric offsets of the NuSTAR NEP-TDF survey could not be measured reliably due to the limited number of bright sources in the field, but the previous NuSTAR COSMOS survey (Civano et al. 2015) found a NuSTAR astrometric offset of $1''$ – $7''$, small compared to the NuSTAR FWHM. Therefore, astrometric offsets should only marginally affect our results (Civano et al. 2015), and we did not apply any astrometric correction when merging the observations. (In any case, there is only one bright source in the FoV that could have been used for astrometric correction.) Figure 2 shows the 3–24 keV FPMA+B merged mosaics.

2.4. Background Map Production

The background map was used for both source detection and simulation. The background of NuSTAR is spatially non-uniform across the field of view (FoV) and is

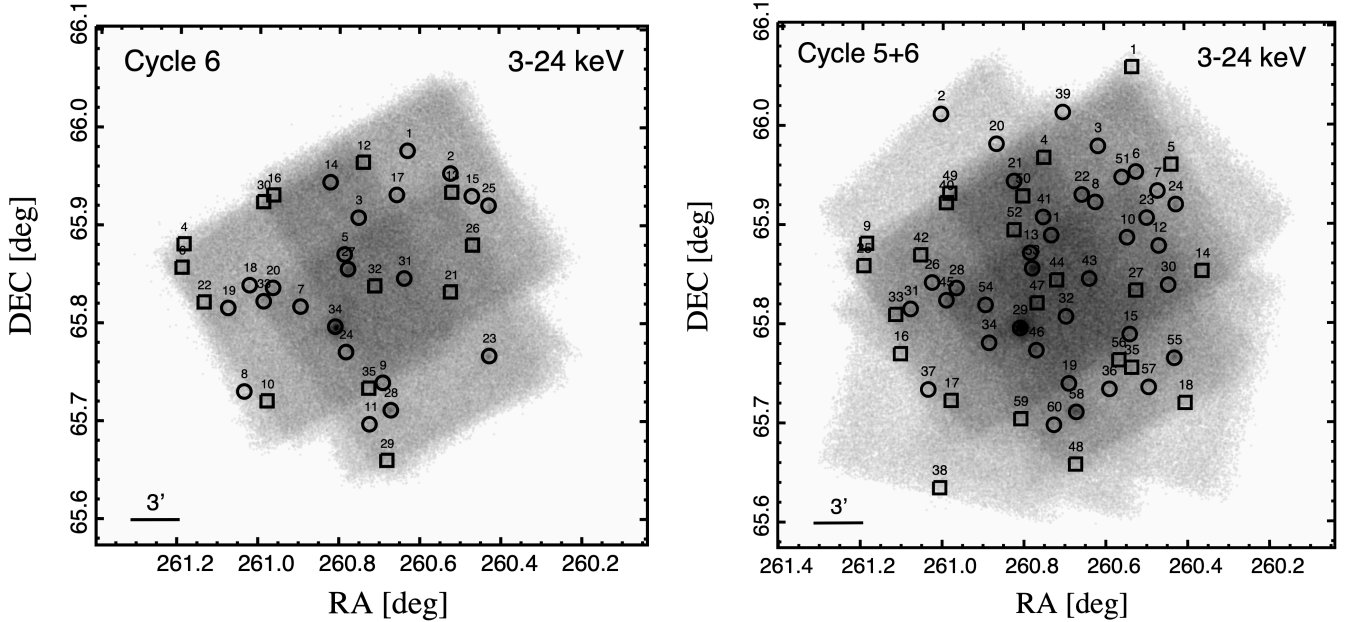


Figure 2. NuSTAR FPMA+B 3–24 keV mosaics of cycle 6 (left) and cycles 5+6 (right) observations. The NuSTAR-detected sources with (black circles, 25'' radius) and without (black squares, 45'' width) soft X-ray counterparts are marked. Labels are source IDs in the respective catalogs.

variable among different observations, adding complexities when producing the background maps. We used the `nuskybgd`³ package (Wik et al. 2014), which was used for all previous NuSTAR extragalactic surveys, to produce background maps of each cycle 6 observation following the same method as Z21. We merged the cycle 6 background maps into an FPMA+B mosaic, which was then merged with the cycle 5 mosaic into a cycles 5+6 mosaic.

To test the accuracy of the generated background maps, we compared the number of counts in the observed images and the corresponding background maps. As the background dominates the observation in most areas, the observed numbers of counts should be consistent except for the regions where (bright) X-ray sources exist. The comparison was based on 64 circular, 45''-radius regions across the FoV in each observation, and the mean difference between the observed images (Data) and the background maps (Bgd) is $(\text{Data} - \text{Bgd})/\text{Bgd} = -0.7\%$ and 2.0% for FPMA and FPMB, respectively. The standard deviations of the differences are 12.2% and 13.8% for FPMA and FPMB, respectively. These suggest good modeling of the NuSTAR background and are consistent with the accuracy obtained in cycle 5 (Z21) and by Civano et al. (2015).

3. NuSTAR SIMULATIONS

³ <https://github.com/NuSTAR/nuskybgd>

Comprehensive simulations in each energy band (3–24 keV, 3–8 keV, 8–24 keV, 8–16 keV, and 16–24 keV) were used to (1) determine the reliability and completeness of our source detection technique and the resulting source catalogs, (2) measure the sensitivity of the surveys, and (3) demonstrate the quality of our source detection technique by comparing the input and measured source properties (e.g., positions and fluxes).

3.1. Generating Simulated Observations

We generated simulated observations in the five energy bands following Z21’s procedure. To summarize, each iteration randomly places mock sources on the background maps described in Section 2.4. The fluxes of the mock sources were randomly assigned following the X-ray source flux distribution ($\log N - \log S$) measured by Treister et al. (2009). The minimum fluxes in the 3–24 keV bands were $3 \times 10^{-15} \text{ erg cm}^{-2} \text{ s}^{-1}$ for cycle 6 and $2 \times 10^{-15} \text{ erg cm}^{-2} \text{ s}^{-1}$ for cycle 5+6, about 10 times fainter than the expected limits of each survey. Adopting a much fainter flux limit than the sensitivity of the survey would result in many mismatched measured and input sources and produce an incorrect reliability curve of source detection. The fluxes of the input sources in each energy band were extrapolated from their 3–24 keV fluxes assuming an absorbed power-law model with photon index $\Gamma = 1.80$ and a Galactic absorption $N_{\text{H}} = 3.4 \times 10^{20} \text{ cm}^{-2}$ (HI4PI Collaboration et al. 2016). The fluxes were converted to count rates using conversion factors (CF) of 4.86, 3.39, 7.08, 5.17, and

Table 3. Source detections in simulated and real data

	3–24 keV	3–8 keV	8–24 keV	8–16 keV	16–24 keV	
Cycle 6						
Simulations						
Detections in each simulated map	53	51	49	49	43	
Detections matched to input catalog	38	36	29	29	16	
DET_ML>95% reliability threshold	20.9	17.4	8.2	9.0	0.6	
Real Data						Total
DET_ML>95% reliability threshold	28	24	13	15	3	35
Cycles 5+6						
Simulations						
Detections in each simulated map	80	78	74	72	63	
Detections matched to input catalog	57	53	43	44	24	
DET_ML>95% reliability threshold	32.9	27.7	14.1	15.9	1.3	
Real Data						Total
DET_ML>95% reliability threshold	45	32	24	26	2	60

NOTE—The mean number of the detected sources using **SExtractor** in each simulated map (line 1). The mean number of the detected sources matched the input source catalog within 30'' (line 2). The mean number of the detected sources with DET_ML above 95% reliability threshold in the simulated maps (lines 3) and the real data (lines 5).

$16.2 \times 10^{-11} \text{ erg cm}^{-2} \text{ count}^{-1}$ in the 3–24, 3–8, 8–24, 8–16, and 16–24 keV bands, respectively. The CF was computed using WebPIMMS⁴ assuming the above spectral model. The simulated observations of each exposure were then merged into mosaics in five energy bands for both FPMA and FPMB, which were then combined into FPMA+B mosaics. We used 1200 simulations for the NuSTAR NEP-TDF cycle 6 survey and 2400 for the combined cycles 5+6 survey.

3.2. Source Detection on Simulated Observations

We performed source detection on the simulated cycle 6 and cycles 5+6 FPMA+B mosaics using the technique developed by Mullaney et al. (2015). In summary, source detection used **SExtractor** (Bertin & Arnouts 1996) on the false-probability maps produced by the simulated observations and background maps. We defined the maximum likelihood (DET_ML) of each detection, which measured the chance that the detection is from the background fluctuation rather than from a real source. A higher DET_ML suggests a lower chance that the detection is from the background fluctuation. Further details were described by Z21.

The measured counts associated with a detected source might be contaminated by other sources within 90'', corresponding to 85–90% encircled energy fraction

(EEF) of the NuSTAR point spread function (PSF). Therefore, we applied a deblending process to the detected sources in each simulation following Mullaney et al. (2015). The deblended source counts and background counts were then used to update DET_ML values for each detection.

The detections with the updated DET_ML of each simulation were then matched with the input catalog using a 30'' search radius. The average numbers of the sources detected and matched to the input catalogs in each simulation are listed in Table 3.

3.3. Reliability and Completeness

To evaluate the accuracy and efficiency of the source detection in the real observations, we used the statistics of the simulated sources described in Section 3.2. Reliability is the ratio of true detections, i.e., matching input sources, to the total number of detected sources at or above a particular DET_ML threshold:

$$\text{Rel}(\text{DET_ML}) = \frac{N_{\text{matched}}(\geq \text{DET_ML})}{N_{\text{detected}}(\geq \text{DET_ML})} \quad (1)$$

Therefore, if 99 out of 100 detected sources with $\text{DET_ML} \geq 15$ were matched to input sources, then the reliability of the detection at $\text{DET_ML} \geq 15$ is 99%. Completeness is defined as the ratio of the number of detected true sources to the number in the input catalog at a particular flux assuming a particular reliability:

$$\text{Completeness}(\text{flux}) = \frac{N_{\text{matched} \& \geq \text{Rel.}(\text{flux})}}{N_{\text{input}(\text{flux})}} \quad (2)$$

⁴ <https://heasarc.gsfc.nasa.gov/cgi-bin/Tools/w3pimms/w3pimms.pl>

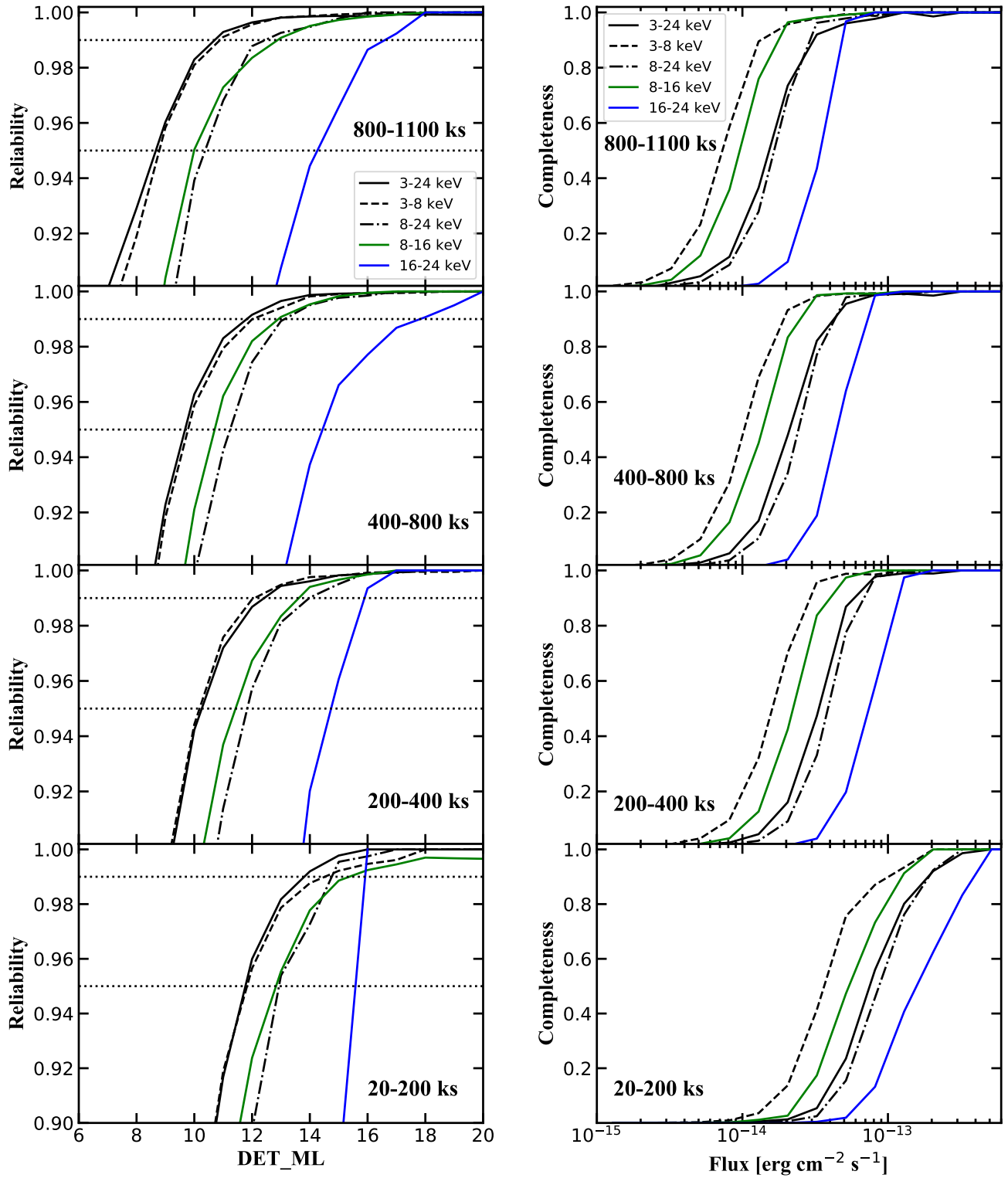


Figure 3. Left column: Reliability (equation 1) as a function of DET_ML. Right column: Completeness (equation 2) at 95% reliability as a function of flux. All values come from the cycle 6 simulations described in Section 3. Panels from top to bottom show four different exposure-time ranges, as labeled. Line types indicate energy ranges as indicated in the legends in the top panels. Dotted horizontal lines in the left panels show 95% and 99% reliability.

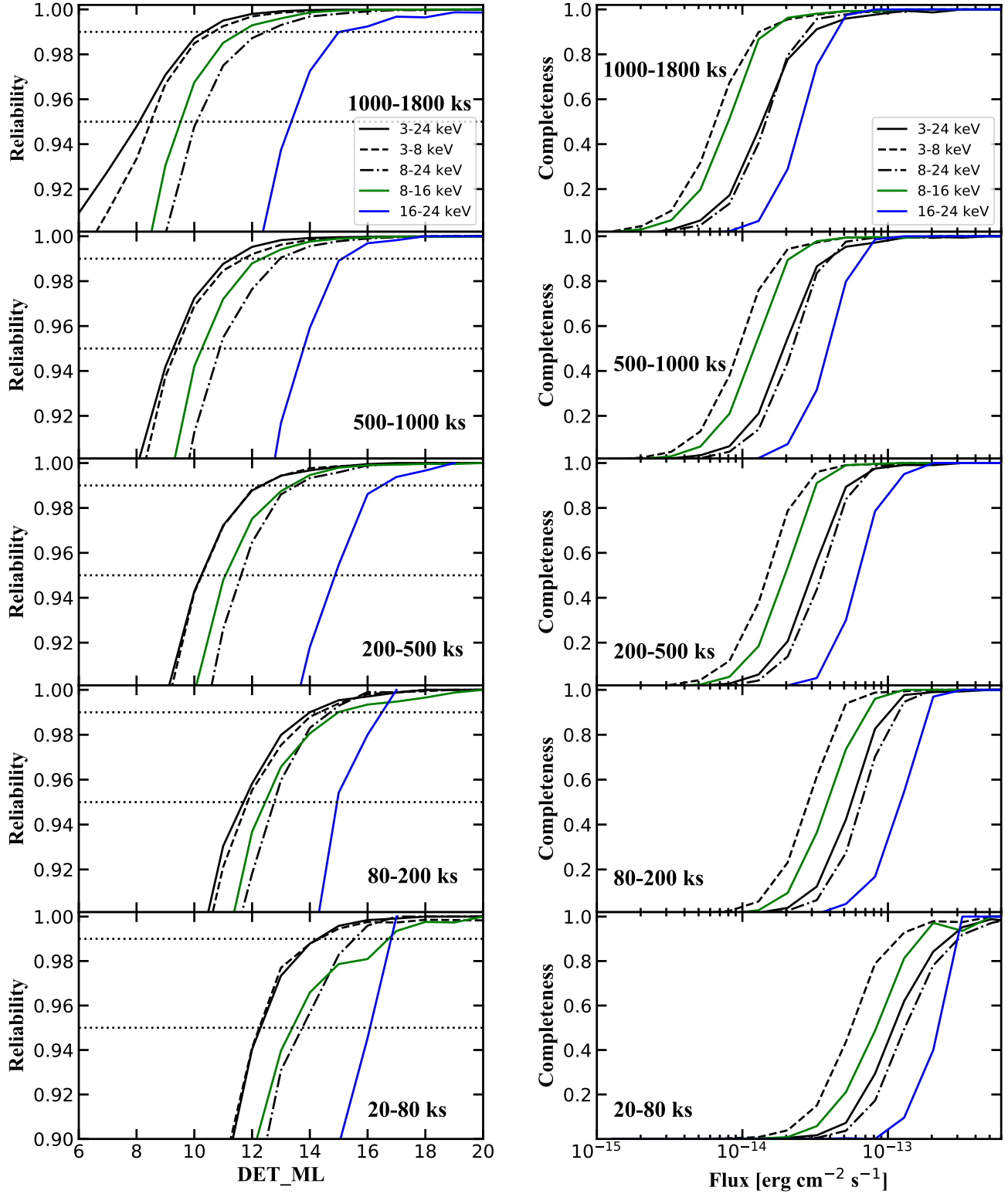


Figure 4. Left column: Reliability (equation 1) as a function of DET_ML. Right column: Completeness (equation 2) at 95% reliability as a function of flux. All values come from the cycle 5+6 simulations described in Section 3. Panels from top to bottom show four different exposure-time ranges, as labeled. Line types indicate energy ranges as indicated in the legends in the top panels. Dotted horizontal lines in the left panels show 95% and 99% reliability.

Table 4. DET_ML values required for 95% reliability

	3–24 keV	3–8 keV	8–24 keV	8–16 keV	16–24 keV
Cycle 6					
DET_ML(20–200 ks) threshold	11.77	11.83	12.93	12.83	15.58
DET_ML(200–400 ks) threshold	10.26	10.18	11.83	11.43	14.74
DET_ML(400–800 ks) threshold	9.68	9.78	11.24	10.70	14.44
DET_ML(800–1100 ks) threshold	8.67	8.79	10.37	9.99	14.26
Cycles 5+6					
DET_ML(20–80 ks) threshold	12.29	12.25	13.74	13.40	16.08
DET_ML(80–200 ks) threshold	11.70	11.85	12.77	12.46	14.95
DET_ML(200–500 ks) threshold	10.24	10.26	11.62	11.08	14.87
DET_ML(500–1000 ks) threshold	9.28	9.40	10.88	10.26	13.78
DET_ML(1000–1800 ks) threshold	8.10	8.50	10.08	9.53	13.36

Therefore, if 90 out of 100 input sources at flux $1 \times 10^{-13} \text{ erg cm}^{-2} \text{ s}^{-1}$ were detected above the 95% reliability level, then the completeness of the survey at this particular flux is 90% at the 95% reliability level. A higher reliability level requires a higher DET_ML threshold, but that leads to lower completeness. Reliability and completeness curves obtained from the cycle 6 and cycles 5+6 simulations are plotted in Figures 3 and 4, respectively.

The reliability and completeness curves heavily depend on the effective exposure time because the spurious detection rate at a given threshold decreases exponentially with exposure. As in cycle 5, the effective exposure time across the entire NEP-TDF cycle 6 and cycles 5+6 survey area is nonuniform (Figure 1) because of the observing strategy. We therefore analyzed the reliability function in different exposure intervals as given in Table 4. The exposure intervals were selected to keep a similar number of detected sources in each interval to achieve similar statistics, and we chose an exposure cut-off at 20 ks to avoid potentially spurious detections on the edge of the observations. Table 3 reports the average number of sources detected at >95% reliability level in each simulation.

3.4. Sensitivity Curves

The effective sky coverage of the survey at a particular flux is the completeness at that flux multiplied by the maximum covered area. For instance, if a survey covering 0.1 deg^2 has 80% completeness at a particular flux, the survey’s effective area at that flux is 0.08 deg^2 . As sensitivity depends on the exposure time, the effective sky coverage of the NEP-TDF survey was calculated by adding up the sky-coverage curves of all different exposure intervals (Table 5). The effective sky-coverage

Table 5. Areas covered with different exposure times

Cycle 5		Cycle 6		Cycles 5+6	
Exposure ks	Area deg^2	Exposure ks	Area deg^2	Exposure ks	Area deg^2
20–200	0.091	20–200	0.026	20–80	0.034
200–500	0.047	200–400	0.037	80–200	0.030
500–700	0.019	400–800	0.030	200–500	0.033
		800–1100	0.014	500–1000	0.033
				1000–1800	0.031

NOTE—Exposure times are vignetting-corrected times for FPMA+B in the 3–24 keV band.

curves in the five energy bands of cycle 6 and cycles 5+6 surveys are plotted in Figure 5. The half-area and 20%-area sensitivity of the three surveys in different energy bands are reported in Table 6.

Observations in the 8–24 keV band are unique to NuSTAR. Therefore, Figure 6 compares the 8–24 keV sensitivities of the cycle 5, cycle 6, and cycles 5+6 NEP-TDF surveys with previous NuSTAR surveys. NEP-TDF currently reaches the deepest flux in a contiguous NuSTAR survey.

3.5. Positional Uncertainty

The simulations described in Section 3.1 can quantify the positional uncertainties of the sources detected. Figure 7 shows the separations between the detected and input-catalog positions in the cycles 5+6 survey simulations as an example. The separation histograms follow a Rayleigh distribution (Pineau et al. 2017). The best-fit Rayleigh scale parameter for all matched sources are $\sigma_{\text{all,C6}} = 9''.5$ and $\sigma_{\text{all,C56}} = 9''.2$ for cy-

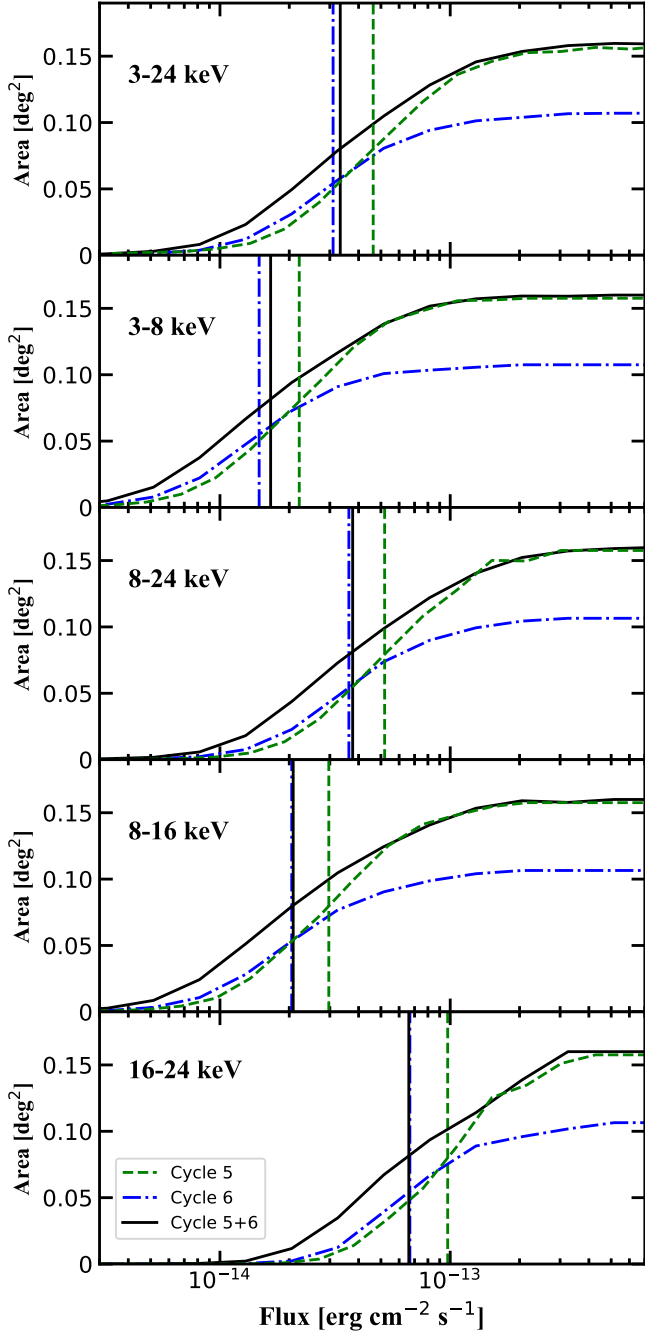


Figure 5. Sky coverage as a function of flux at the 95% reliability level. Panels from top to bottom are for the five energy bands as labeled. As indicated in the legend, different line types show different survey components. The vertical dashed line shows the half-area flux of each survey component. (At the highest energies, the cycle 5 and cycle 6 lines overlap.)

cle 6 and cycles 5+6 surveys, respectively. Eliminating the faintest sources by limiting the sample to sources detected above the 95% reliability level gives smaller separations $\sigma_{95\%,C6} = 6''.6$ and $\sigma_{95\%,C56} = 6''.5$.

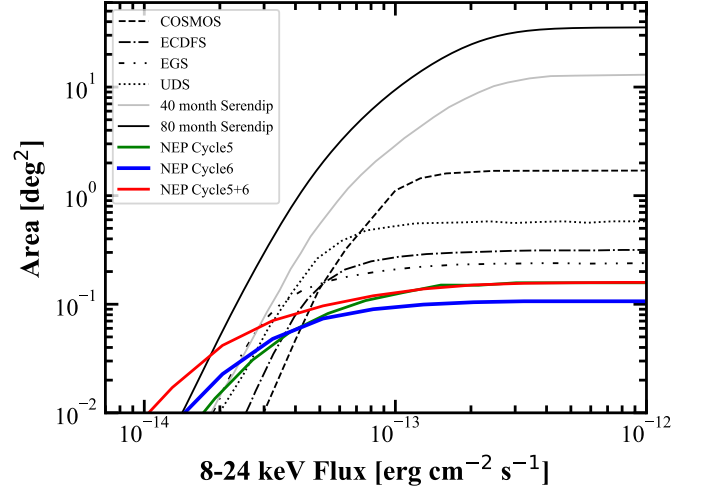


Figure 6. 8–24 keV sky coverage as a function of flux in NuSTAR surveys. Different line types represent different NuSTAR extragalactic surveys as indicated in the legend.

Table 6. NuSTAR Survey Sensitivities

Energy (keV)	Half-area	20%-area
NuSTAR	Cycle 5/6/5+6	Cycle 5/6/5+6
	$10^{-14} \text{ erg cm}^{-2} \text{ s}^{-1}$	$10^{-14} \text{ erg cm}^{-2} \text{ s}^{-1}$
3–24	4.6/3.1/3.3	2.4/1.7/1.6
3–8	2.2/1.5/1.7	1.1/0.80/0.74
8–24	5.2/3.6/3.8	2.7/2.0/1.7
8–16	3.0/2.1/2.1	1.5/1.1/0.95
16–24	9.8/6.7/6.6	5.2/3.9/3.1
XMM-Newton	Cycle 6	Cycle 6
	$10^{-15} \text{ erg cm}^{-2} \text{ s}^{-1}$	$10^{-15} \text{ erg cm}^{-2} \text{ s}^{-1}$
0.5–2	0.87	0.63
2–10	6.3	4.0

NOTE—Sensitivities are shown for half and for 20% of the maximum survey area in all relevant energy bands.

The separations are even smaller for sources with 3–24 keV flux $>10^{-13} \text{ erg cm}^{-2} \text{ s}^{-1}$, $\sigma_{95\%,\text{bright},C6} = 3''.8$ and $\sigma_{95\%,\text{bright},C56} = 3''.7$. The measured separations are consistent with the previous cycle 5 survey and other NuSTAR extragalactic surveys, and therefore we used these distributions as the expected positional uncertainty of real detections. The simulations did not include the astrometric offsets, and therefore they do not reflect the full positional uncertainty, but the effect is likely minimal.

3.6. Fluxes

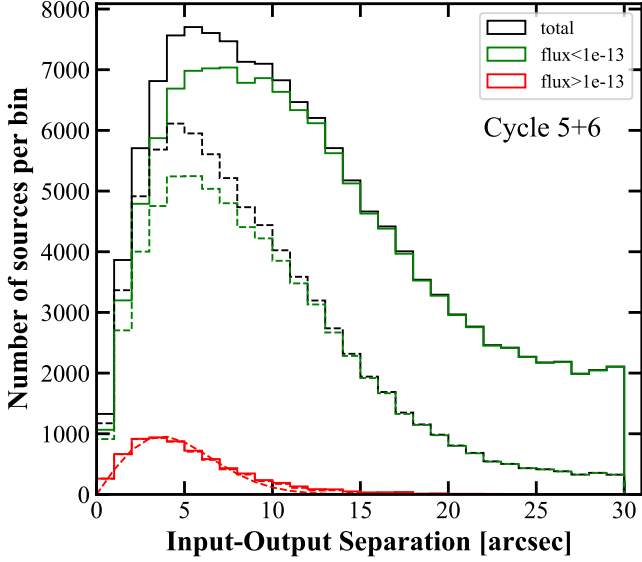


Figure 7. Distributions of position offsets from the NuSTAR simulations of the 3–24 keV cycles 5+6 survey. Solid lines refer to the whole sample and dashed lines refer only to sources above the 95% reliability level. The dashed red curve shows the best Rayleigh fit to the offsets of sources above the 95% reliability level.

The fluxes of the simulated sources detected in each energy band were measured and compared with the input fluxes to quantify the accuracy of the flux measurement technique. We extracted the source counts and deblended background counts of each matched source using the CIAO (Fruscione et al. 2006) tool `dmextract`. The effective exposure of each source was measured from the exposure maps (Section 2.2). The net counts were then converted to in-band fluxes using the CF (Section 3.1). The counts were extracted in a $20''$ circular region, and we converted this aperture flux to total flux using an aperture correction factor of $F(20'')/F_{\text{tot}} = 0.32$, as calculated from the NuSTAR PSF.⁵ Figure 8 shows the ratio of measured to input 3–24 keV fluxes. Flux measurements for faint sources are over-estimated, as expected from Eddington bias which favors the detection of faint sources with positive noise deflections. This excess corresponds to the detection limits of the survey and is also exposure-dependent (Figure 4). Therefore, the fluxes of the fainter sources can be better measured with deeper exposures.

Z21 found an under-estimate of the measured fluxes for bright ($F_{3-24} > 10^{-12} \text{ erg cm}^{-2} \text{ s}^{-1}$) sources. This

⁵ https://heasarc.gsfc.nasa.gov/docs/nustar/NuSTAR_observatory_guide-v1.0.pdf

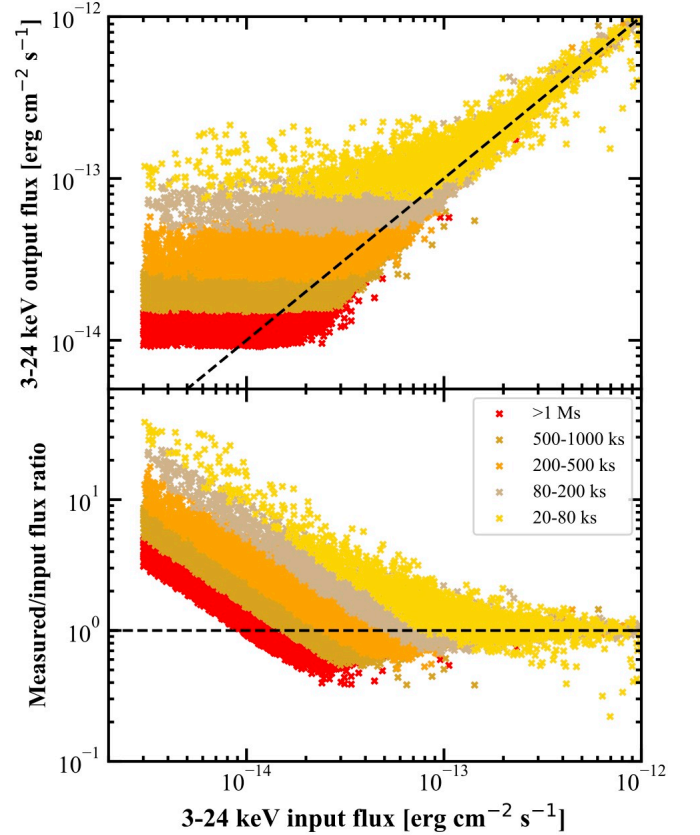


Figure 8. Upper: Measured versus input 3–24 keV fluxes for simulated sources. Lower: ratio of measured to input fluxes for the same sources. Both panels show only sources above the 95% reliability level of the cycles 5+6 survey. Sources in different exposure intervals are plotted in different colors as indicated in the legend. Dashed lines in both panels show equality. The excess at lower fluxes is due to the Eddington bias.

was due to a computing error when generating false probability maps where the false probability in the center pixel of the bright sources was saturated. The bug led to an incorrect measurement of the source position and therefore underestimating its flux. This error did not affect the flux measurement of the real observations in the NEP-TDF because all detected sources are much fainter than $10^{-12} \text{ erg cm}^{-2} \text{ s}^{-1}$. The error is fixed in this work.

4. NuSTAR SOURCE CATALOG

To maximize the signal-to-noise ratio (SNR), we performed source detections on the FPMA+B mosaics of the actual NuSTAR observations in the cycle 6 and cycles 5+6 surveys using the same detection strategy as in the simulations (Section 3.2). Source detection, requiring DET_ML above the 95% reliability level, was performed separately in each of the five energy bands. The

resulting coordinates, source counts, background counts, DET_MLs, and vignetting-corrected exposure times of the detected sources were then merged into a master catalog by using a 30'' matching radius among the five energy bands. The master catalog therefore includes all sources detected in at least one energy band above the 95% reliability level. The coordinates of the sources reported in the master catalog are taken from the detections that have the highest DET_ML among the five energy bands. The positions of the sources detected in cycle 6 and cycles 5+6 surveys are plotted in Figure 2.

The master catalog includes 35 and 60 sources for cycle 6 and cycles 5+6 surveys, respectively. The number of the sources detected above 95% reliability level in each energy band and the merged master catalog are listed in Table 3. Statistically, we expect about two to three spurious detections in the 95% reliability master catalogs. Table 7 reports the number of sources detected in each combination of energy bands.

Figure 9 shows the distribution of the source fluxes in different energy bands from the various master catalogs. The source fluxes were calculated with the method described in Section 3.6. For sources not detected in an energy band, background counts were not deblended. We calculated 1σ net count-rate and flux uncertainties for the sources that were detected above the 95% reliability level in a given energy band using Equations (9) and (12) of [Gehrels \(1986\)](#) with $S = 1$. For sources not detected above the 95% reliability level, we calculated the 90% confidence level upper limits of net count-rates and fluxes using Equation (9) of [Gehrels \(1986\)](#) with $S = 1.645$.

The master catalogs of the NuSTAR detected sources in cycle 6 and cycles 5+6 surveys are made public with this paper. Table 9 explains each column in the catalogs.

Variability detection is the prime goal of the NuSTAR NEP-TDF survey. We developed a dedicated pipeline, briefly introduced in Appendix APPENDIX D, using a Bayesian method to analyze the source variability in NuSTAR observations. As a preliminary result, four sources showed variability in cycles 5+6 at $p < 0.05$ ($\sim 2\sigma$) in at least one energy band in the 26-months of observations. Systematic discussion of source variability in the NuSTAR and XMM-Newton NEP-TDF will be presented in future work.

5. XMM-NEWTON NEP-TDF SURVEY

To provide lower-energy (0.5–10 keV) information, XMM-Newton observed the NEP-TDF field simultaneously with the four cycle 6 NuSTAR epochs. The observations utilized all three XMM-Newton cameras, i.e., MOS1, MOS2, and pn. Unfortunately, the entire 16 ks

Table 7. Energy bands of detected sources

Energy	Cycle 5	Cycle 6	Cycles 5+6
F+S+H	9 (27%)	13 (37%)	17 (28%)
F+S+h	6 (18%)	4 (11%)	5 (8%)
F+S	1 (3%)	2 (6%)	4 (7%)
F+s+H	0 (0%)	2 (6%)	2 (3%)
F+s+h	5 (15%)	5 (14%)	12 (20%)
F+s	3 (9%)	0 (0%)	0 (0%)
F+H	0 (0%)	2 (6%)	2 (3%)
F+h	2 (6%)	0 (0%)	1 (2%)
F	0 (0%)	0 (0%)	1 (2%)
f+S+h	1 (3%)	1 (3%)	1 (2%)
f+S	1 (3%)	2 (6%)	3 (5%)
f+s+H	1 (3%)	0 (0%)	3 (5%)
f+H	2 (6%)	1 (3%)	2 (3%)
S+h	0 (0%)	1 (3%)	1 (2%)
S	1 (3%)	1 (3%)	1 (2%)
H	1 (3%)	1 (3%)	5 (8%)
Total	33	35	60

NOTE—Numbers are for the master catalogs for cycle 5 (Z21), cycle 6, and cycles 5+6 surveys. F(f), S(s), and H(h) represent the full (3–24 keV), soft (3–8 keV), hard (8–24 keV and/or 8–16 keV and/or 16–24 keV) energy bands. F, S, and H represent sources detected above the 95% reliability threshold in the given energy band, while f, s, and h refer to the sources detected below the 95% reliability threshold.

of data in the third epoch were lost to high particle background. Otherwise, each XMM-Newton epoch had exposure time ~ 20 ks, and the total effective exposure time is 62 ks. Details are in Table 2. The XMM-Newton observations cover a field of 0.21 deg^2 , about 90% of the NuSTAR NEP-TDF field. The two missing bottom corners of the field (Figure 10) contain one NuSTAR source (ID 38).

5.1. Data Reduction

The XMM-Newton data were reduced following [Brunner et al. \(2008\)](#); [Cappelluti et al. \(2009\)](#); [LaMassa et al. \(2016\)](#); and [Z21](#). Details of the XMM-Newton Science Analysis System (SAS) packages are described in the XMM-Newton data analysis threads.⁶ The observational data files (ODFs) of MOS1, MOS2, and pn were generated using the SAS version 20.0.0 tasks `emproc` and `epproc`. High-background time intervals of the three instruments were excluded using $>10 \text{ keV}$ count-rate thresholds of 0.2 and 0.3 counts s^{-1} for MOS

⁶ <https://www.cosmos.esa.int/web/xmm-newton/sas-thread-src-find-stepbystep>

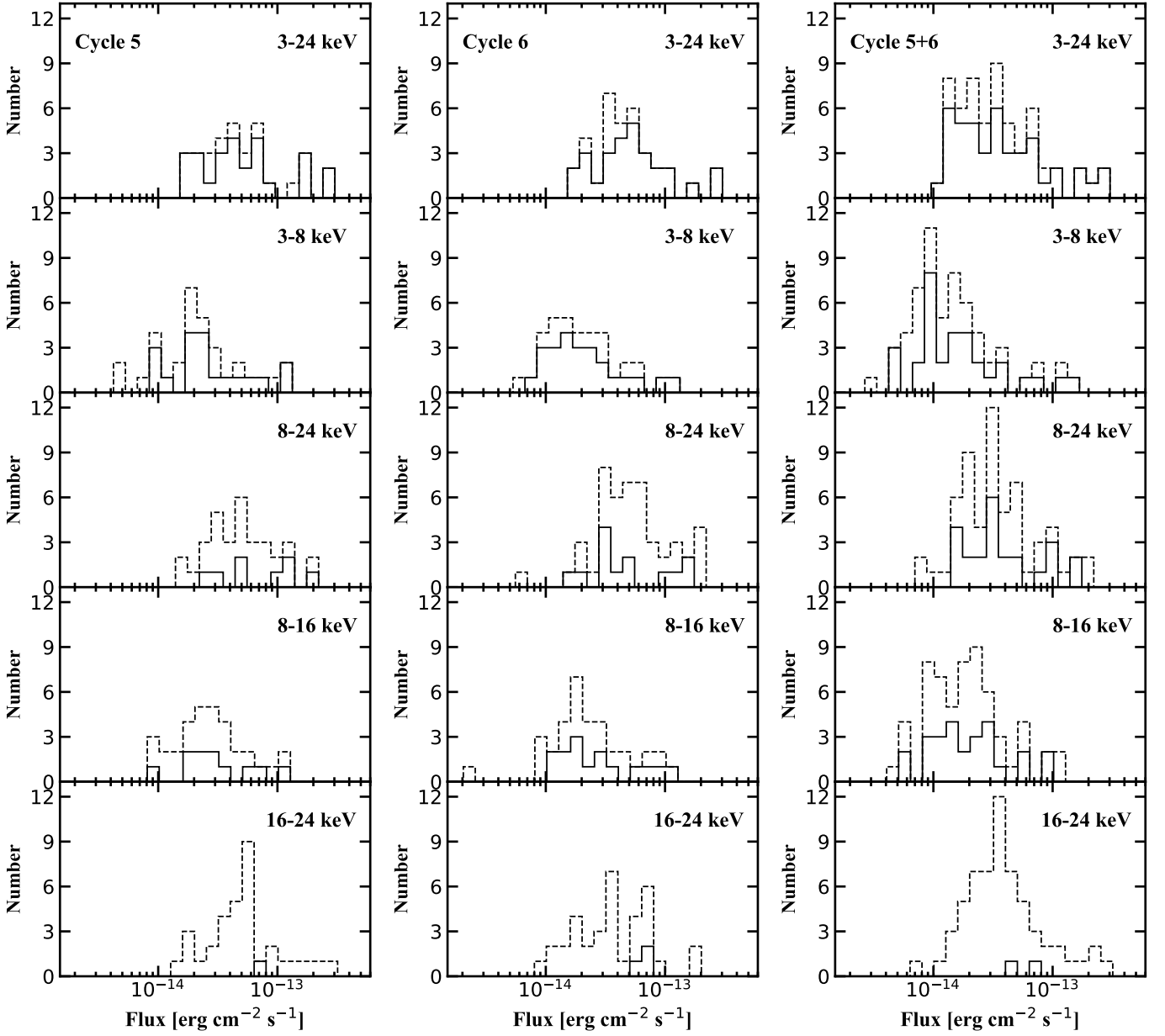


Figure 9. Flux distributions of NuSTAR sources. Panels from left to right show results for the cycle 5 (Z21), cycle 6, and cycles 5+6 surveys, respectively. Panels from top to bottom show different energy bands as labeled in each panel. Solid lines represent sources detected above the 95% reliability level in the specific survey and band, and dashed lines represent all 60 sources detected by NuSTAR. For sources not detected in a particular survey and energy range, the flux plotted is the 90%-confidence upper limit.

and pn, respectively. We also excluded data in energy bands that might be contaminated by fluorescent emission lines, i.e., the Al $K\alpha$ line at 1.48 keV in both MOS and pn and two Cu lines at ~ 7.4 keV and 8.0 keV only in pn. The specific energy intervals removed were 1.45–1.54 keV in both MOS and pn data and 7.2–7.6 keV and 7.8–8.2 keV in pn. We then used the clean event files to generate the images of MOS 1,2 and pn in the 0.5–2 keV and 2–10 keV bands.

To generate exposure maps, we used the SAS task `eexmap`. The maps were weighted by each instrument’s energy conversion factor (ECF), which converts count rate to flux. ECFs were calculated using WebPIMMs assuming an absorbed power-law model with $\Gamma = 1.80$ and Galactic column density $N_H = 3.4 \times 10^{20} \text{ cm}^{-2}$, as for the NuSTAR observations (Section 3.1). The ECFs used for MOS and pn are 0.54 and $0.15 \times 10^{-11} \text{ erg cm}^{-2} \text{ count}^{-1}$ in the 0.5–2 keV band, and 2.22 and $0.85 \times 10^{-11} \text{ erg cm}^{-2} \text{ count}^{-1}$ in the 2–10 keV band, respectively.

Background maps were generated for each instrument after masking detected sources. Preliminary source detection used a sliding-box method with SAS package `eboxdetect` and detection likelihood `LIKE` set to >4 to avoid any possible sources. (The detection likelihood is defined as $\text{LIKE} \equiv -\ln p$, where p is the probability of a Poissonian random fluctuation of the counts in the detection box which would have resulted in at least the observed number of source counts.) We generated the background map using SAS package `espinemap` assuming a 2-component model of the XMM-Newton background by setting `fitmethod = model`. This 2-component model considers background from both the detector (particles) and the CXB.

5.2. Source Detection

To maximize sensitivity, we co-added the cleaned images, exposure maps, and background maps of the three instruments into mosaic images for the two energy bands using the SAS `emosaic` task. Figure 10 shows the merged mosaic. Source detection was performed using the SAS `eboxdetect` and `emldetect` tasks, the latter to optimize detection of the center of the source. Source detection was performed in the 0.5–2 keV and 2–10 keV bands simultaneously to minimize uncertainties in source positions and fluxes. A detection required `mlmin` >6 in either of the two bands. This threshold corresponds to a reliability of 97.3% in the 0.5–2 keV band and 99.5% in the 2–10 keV band based on simulations of the XMM-COSMOS survey (Cappelluti et al. 2007), which has a ~ 60 ks depth similar to the XMM-Newton

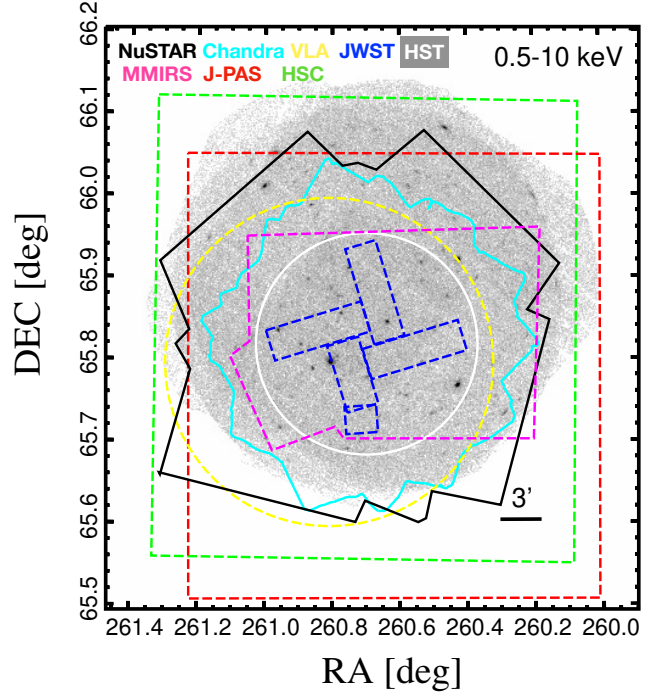


Figure 10. XMM-Newton MOS+pn mosaics combining 0.5–10 keV observations from all three epochs. The footprints of other surveys in the NEP-TDF field are plotted in different colors as indicated in the key. SDSS and WISE catalogs cover the entire XMM and NuSTAR regions.

NEP-DTF survey. Source detection excluded the margin of the FoV where the exposure time is <1 ks.

5.3. Astrometric Correction and Uncertainty

Before merging the three epochs of observations into mosaics to maximize the sensitivity of the survey, we estimated the astrometric offsets of the three observations. The astrometric offset of an XMM-Newton observation is typically less than $3''$ and on average is $1''.0$ – $1''.5$ (e.g., Cappelluti et al. 2007; Ni et al. 2021). To determine the astrometric offset of our three epochs, we matched $>6\sigma$ (`mlmin` >20) XMM-Newton sources to optical sources from the Sloan Digital Sky Survey (SDSS) DR16.⁷ Only `Type = Star` sources were used, and the matching radius was $4''.5$. XMM-Newton epochs 1, 2, and 4 had 13, 22, and 15 matched SDSS counterparts, respectively. The median offsets in R.A. and Decl. are $(\Delta\alpha, \Delta\delta) = (3''.97, 0''.95)$ for epoch 1, $(0''.88, 1''.13)$ for epoch 2, and $(0''.06, 1''.46)$ for epoch 4. We applied these offsets to the event and attitude files in each observation and remade the images, background maps, and exposure maps with the corrected files.

⁷ <https://www.sdss4.org/dr16/>

To test the astrometric corrections, we performed the source detection again and measured the offsets of the same sources from their optical counterparts. The average XMM-Newton to SDSS separations were reduced by 30% for epoch 1, 45% for epoch 2, and 41% for epoch 4 after the astrometric correction. Furthermore, the median XMM-Newton offsets among different epochs decreased by 84%–96%, suggesting that the three epochs became better aligned. The resulting images, background maps, and exposure maps of the three epochs were then merged into mosaics. The new images have more high-count pixels than the old images, again suggesting that the alignment is better corrected. The new average X-ray-to-optical offset is $1''.22$, and we take this to be the systematic position uncertainty of the XMM-Newton NEP-TDF survey.

5.4. Sensitivity

The sensitivity curves of the XMM-Newton NEP-TDF survey are plotted in Figure 11. The sensitivity maps were generated using the SAS `esensmap` package assuming a maximum likelihood $m_{\text{lmin}} > 6$. The half-area and 20%-area sensitivities are reported in Table 6.

5.5. XMM-Newton Source Catalog

The final XMM-Newton NEP-TDF catalog includes 194 sources in the 0.5–2 keV band and 172 sources in the 2–10 keV band at $m_{\text{lmin}} > 6$. There were only 80 sources in common in the two bands giving a total of 286 individual sources detected in at least one band. The source properties are listed in the XMM-Newton source catalog, and descriptions of each column of the catalog are in Table 10. The source flux distributions are plotted in Figure 12.

5.6. Cross-match with NuSTAR

We cross-matched the XMM-Newton sources with the 60 sources detected in the NuSTAR cycles 5+6 survey using a simple position match. The match radius was the $20''$ NuSTAR position uncertainty combined in quadrature with the position uncertainty of individual XMM-Newton sources (σ_{XMM} from the `emldetect` best-fit results) and the $1''.22$ XMM-Newton systematic uncertainty. The $20''$ NuSTAR uncertainty is three times the best-fit Rayleigh scale parameter ($\sigma_{95\%, \text{C56}} = 6''.5$) of the simulated position errors (Section 3.5). In all, 36 NuSTAR sources match at least one XMM-Newton counterpart. Thirty of these have a single XMM-Newton counterpart, and six (ID 11/13/23/31/41/46) have two XMM-Newton counterparts within the search radius. In all six cases, one of the XMM-Newton sources is both brighter and closer to the NuSTAR position than the

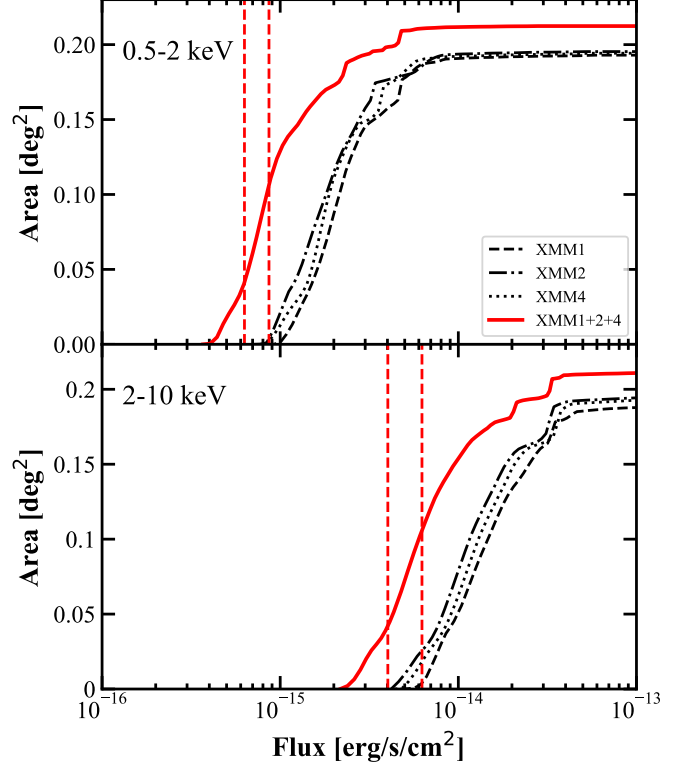


Figure 11. XMM-Newton NEP-TDF sensitivity maps. The upper panel shows 0.5–2 keV, and the lower shows 2–10 keV. Different line types show different epochs as indicated in the legend. Vertical dashed lines show the half-area and 20%-area sensitivities for the three epochs combined.

other, and we took this to be the primary counterpart. One NuSTAR source (ID 51) has two XMM-Newton sources (ID 134/181) just outside the search radius ($22''.8$ and $23''.3$, respectively). The two are in opposite directions and were both detected in the 2–10 keV band with similar flux $F(2-10 \text{ keV}) \sim 9 \times 10^{-15} \text{ erg cm}^{-2} \text{ s}^{-1}$. This looks like a case of source confusion where both XMM-Newton sources contribute to the NuSTAR detection.

In all, 37 out of 60 NuSTAR sources have at least one XMM-Newton association. Of the remaining 23, 17 (ID 1/4/5/9/14/16/17/18/40/42/44/47/48/49/50/56/59) were undetected or below the 95% reliability level in the NuSTAR soft 3–8 keV band, suggesting that they might be heavily obscured and therefore detectable only in hard X-rays. The other six sources (ID 25/27/33/35/38/52) were above the 95% reliability level in the 3–8 keV band but do not have XMM-Newton counterparts. They might be variable sources that were bright only in NuSTAR cycle 5, or some of them could be spurious NuSTAR sources. Statistically, only 2–3 spurious detections are expected in the NuSTAR 95%

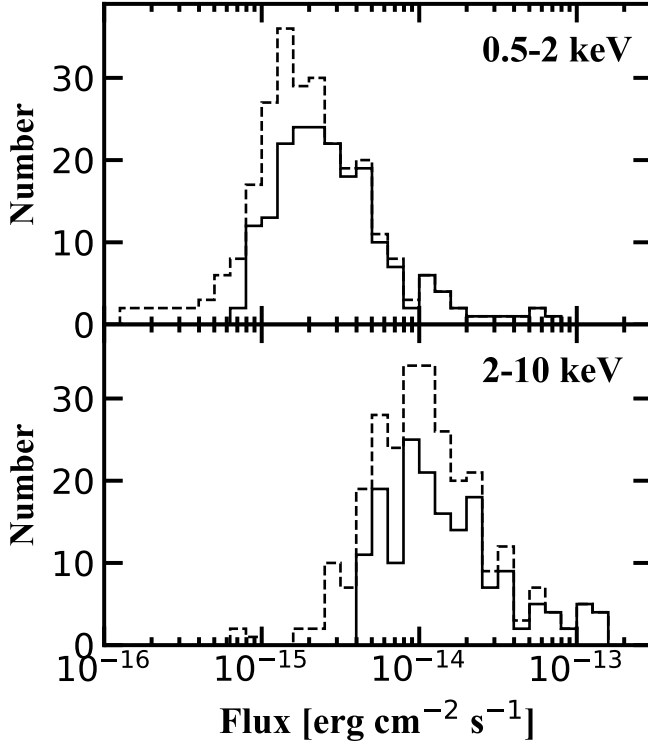


Figure 12. Flux distribution of sources detected in the 0.5–2 keV (top) and 2–10 keV (bottom) bands of the three-epoch combined XMM-Newton mosaic. Solid lines represent the flux distribution of detected sources with $m_{\text{lmin}} > 6$ in a given band. Dashed lines represent the flux distributions of all 286 XMM-Newton sources with those not detected or with $m_{\text{lmin}} \leq 6$ in the given band plotted at their 90% confidence upper limits.

reliability catalog, and therefore variability is likely to be a factor.

For comparison between NuSTAR and XMM-Newton, the XMM-Newton 2–10 keV fluxes were converted to 3–8 keV assuming an absorbed power-law intrinsic SED with photon index $\Gamma = 1.80$ and Galactic absorption $N_{\text{H}} = 3.4 \times 10^{20} \text{ cm}^{-2}$. This gives a conversion factor of 0.62, and Figure 13 shows the comparison. Most sources have comparable fluxes measured by the two observatories. The tendency for NuSTAR fluxes to be higher than XMM-Newton fluxes at the faint end is due to the Eddington Bias as demonstrated by Figure 8. Other offsets could arise from variability in the last three years or different spectral shapes of the sources than assumed for converting the XMM-Newton fluxes to the NuSTAR energy band.

6. MULTIWAVELENGTH COUNTERPARTS

The JWST NEP-TDF has extensive multiwavelength coverage (Windhorst et al. 2023). Because XMM-Newton has a better PSF than NuSTAR, we

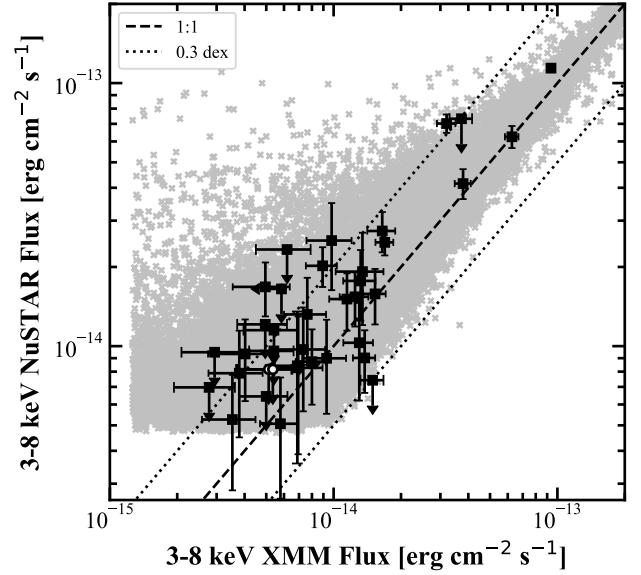


Figure 13. Comparison between NuSTAR and XMM-Newton fluxes for the 37 NuSTAR sources with XMM-Newton counterparts (black filled squares). The dashed line represents the 1:1 relation, and the dotted lines show a factor of two difference. The black open circles show the two XMM-Newton candidate counterparts of NuSTAR ID 51. For undetected sources, the indicated upper limits are 90% confidence. The gray crosses in the background are from the NuSTAR simulations in the 3–8 keV band.

first matched XMM-Newton sources with the visible-wavelength and infrared (IR) catalogs.

6.1. Visible-wavelength Catalogs

We matched X-ray positions to three visible-wavelength catalogs covering the NEP-TDF: SDSS DR17 (Abdurro’uf et al. 2022), the HEROES catalog (Taylor et al. 2023) made from Subaru Hyper Suprime-Cam (HSC; Aihara et al. 2018) images, and the NEP portion (J-NEP; Hernán-Caballero et al. 2023) of the Javalambre-Physics of the Accelerating Universe Astrophysical Survey (J-PAS; Benitez et al. 2014). We used the *i*-band catalogs as they include the largest number of detected sources.

The SDSS catalog covers the entire field, and data were downloaded from the public database.⁸ The HSC images were reduced by S. Kikuta, and the HSC NEP-TDF catalog was generated by C. N. A. Willmer (Willmer et al. 2023). Sources with $m_i < 17.5$ are saturated in the HSC observations, and we replaced their magnitudes with the magnitudes in the SDSS catalog. The J-NEP was performed with the single-CCD

⁸ <https://www.sdss4.org/dr17/>

Pathfinder camera on the 2.55 m Javalambre Survey Telescope (JST) at the Javalambre Astrophysical Observatory with 56 narrow filters and used the SDSS u , g , r , and i filters. J-NEP covered about 80% area of the XMM-Newton field. We applied magnitude cuts at $S/N > 3$ (corresponding to i -band magnitudes $m_i \lesssim 22.5$, 25.8, and 24.5 for SDSS, HSC, and J-PAS, respectively) to the three catalogs to ensure reliable detections and accurate measurements of the source fluxes.

6.2. Infrared Catalogs

We used two near-IR (NIR) catalogs covering the NEP-TDF: the *YJHK* catalog (Willmer et al. 2023) made with the MMT–Magellan Infrared Imager and Spectrometer (MMIRS; McLeod et al. 2012) on the MMT, and the unWISE catalog (Schlafly et al. 2019) made from five years of the Wide-field Infrared Survey Explorer (WISE; Wright et al. 2010) observations. The unWISE wavelengths are 3.4 (W1) and 4.6 μm (W2).

The MMIRS catalog covers 30–40% of the XMM-Newton-observed field, and the $S/N > 3$ sensitivity cuts correspond to $m \lesssim 24.6$, 24.5, 24.1, and 23.5 (in AB magnitudes) in the Y , J , H , and K bands, respectively. The unWISE catalog covers the entire XMM-Newton field, and the $S/N > 3$ sensitivity cuts correspond to $m \lesssim 21.5$ in the W1 band and 20.5 AB in the W2 band.

6.3. Multiwavelength Matching

We used a 5'' matching radius to identify candidate counterparts of the XMM-Newton sources. (More than 95% of XMM-Newton sources are detected within this radius based on the simulations made in the STRIPE 82 XMM-Newton survey: LaMassa et al. 2016.) To choose among possible counterparts within the match radius, we used a maximum likelihood estimator (MLE; Sutherland & Saunders 1992) as applied for X-ray sources detected in previous XMM-Newton and Chandra extragalactic surveys (e.g., Brusa et al. 2007; Civano et al. 2012; Marchesi et al. 2016; LaMassa et al. 2016). These previous results showed >80% reliability. The MLE method considers both the flux and the offset of the candidate counterparts in the context of the position uncertainties of the surveys and the flux distribution of survey sources. The likelihood ratio (LR) that a candidate is the real counterpart is:

$$\text{LR} = \frac{q(m)f(r)}{n(m)} \quad , \quad (3)$$

where m is the catalog magnitude of the candidate, $n(m)$ is the local magnitude distribution of background sources, $q(m)$ is the expected magnitude distribution of the real multiwavelength counterparts, and r is the po-

Table 8. XMM-Newton Match Statistics

Survey	band	XMM	matched	candidates	CP
HSC	i	285	251	514	197
J-PAS	i	261	141	178	131
SDSS	i	286	93	97	93
MMIRS	J	132	125	222	117
WISE	W1	286	210	272	210

NOTE—The four numbers in each row are respectively the number of XMM-Newton sources in the survey’s footprint, the number of those sources with at least one candidate within 5'', the total number of candidates within that area for all sources, and the number of XMM sources with at least one ancillary counterpart (CP) above the chosen LR_{th} .

sition offset between the X-ray source and the candidate. In practice, $n(m)$ was measured in an annulus between 5'' and 30'' from the X-ray source. The function $q(m)$ is the normalization of $q'(m)$, where $q'(m)$ is the magnitude distribution of catalog objects within 5'' of the X-ray source after subtracting $n(m)$ and rescaling to the 5'' circular area. Civano et al. (2012, their Figure 1) gave an example of $q(m)$. The function $f(r)$ is the probability distribution of the positional uncertainties, assumed to be a two-dimensional Gaussian $f(r) = 1/(2\pi\sigma^2) \times \exp(-r^2/2\sigma^2)$, where σ is the quadrature combination of the position uncertainty of the XMM-Newton source (Section 5.6) and the ancillary object (0''.2). The choice of 0''.2 was validated by cross-matching our ancillary table with the extragalactic sources (proper motion $\text{pm} < 10 \text{ mas yr}^{-1}$) in the GAIA DR3 catalog (Gaia Collaboration et al. 2016, 2021). Table 8 lists the number of sources matched by each survey.

We used the LR threshold (LR_{th}) to distinguish whether an ancillary object is the true counterpart of the XMM-Newton detection or is a background source within the search radius. The LR_{th} was determined by balancing the reliability and the completeness of the final selected sample. The reliability and completeness of the matching can be estimated from the survey statistics (Civano et al. 2012). The reliability R_i for an individual candidate j is

$$R_i = \frac{\text{LR}_i}{\sum_i (\text{LR})_i + (1 - Q)} \quad , \quad (4)$$

where Q is the fraction of XMM-Newton sources having at least one candidate counterpart (i.e., the ratio of Table 8 column 4 to column 3). The LR was summed over all potential counterparts within the search radius of a given XMM-Newton source for all ancillary objects within the search radius. The reliability (R) of the entire sample is defined as the ratio between the sum of the re-

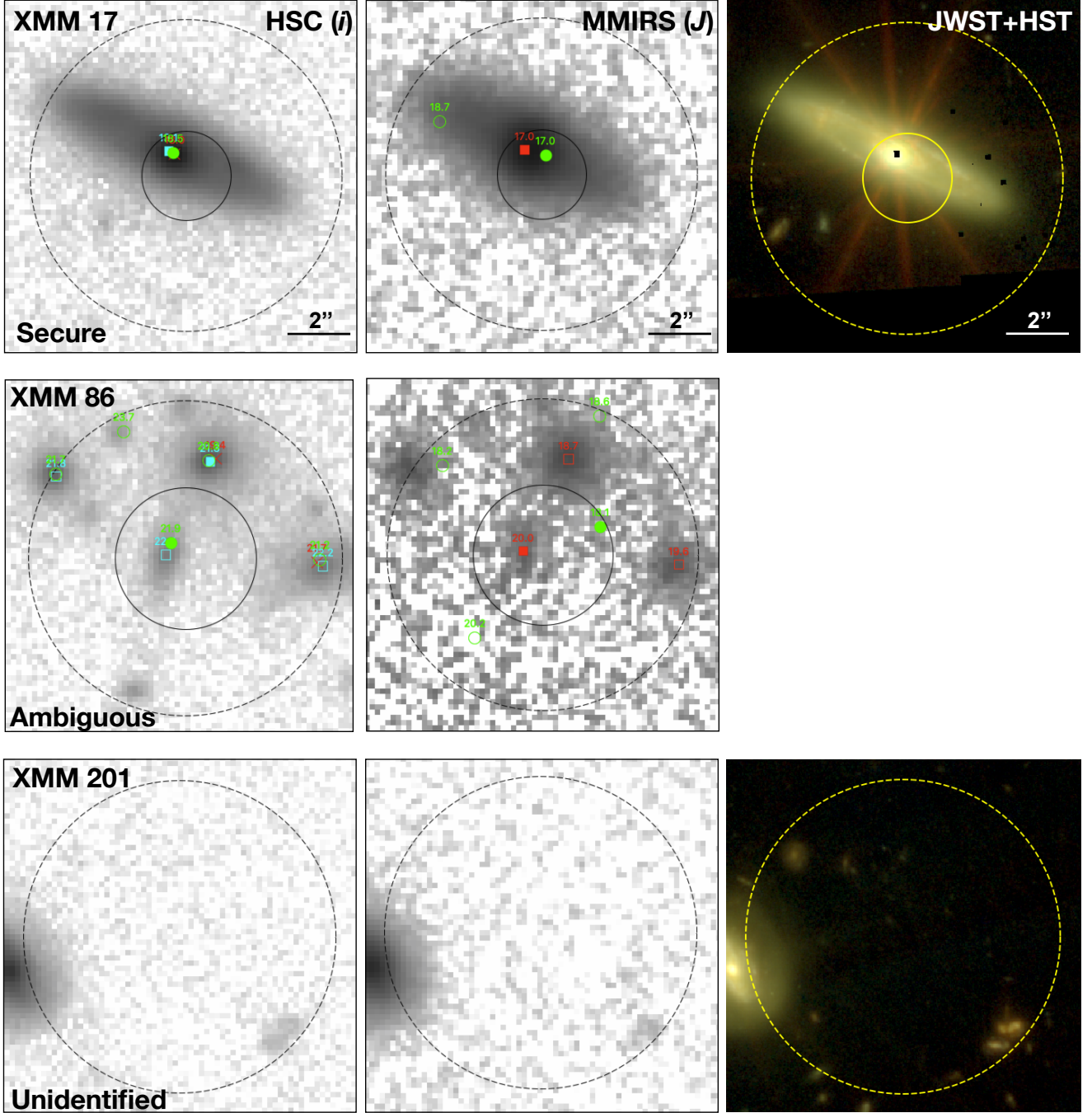


Figure 14. Illustrations of secure (top), ambiguous (middle), and unidentified (bottom) associations of XMM-Newton sources. Negative images left to right are HSC i , MMIRS J , and HST+JWST (11-filter mosaic: HST F275W, F435W, and F606W; JWST F090W, F115W, F150W, F200W, F277W, F356W, F410M, and F444W). All images are oriented north up, east left and centered at the centroid of the XMM-Newton detections. The image scale is indicated in the top row. Solid circles show the XMM-Newton position uncertainty, and dashed circles show the $5''$ matching radius. Labels show i -band magnitudes measured from HSC (cyan square), J-PAS (green circle), or SDSS (red cross) or IR magnitudes measured by MMIRS (J -band, red square) or WISE (W1, green circle). Only ancillary counterparts within the matching radius and with $LR > LR_{th}$ are plotted. The ancillary counterparts with the highest LR are plotted as filled symbols. XMM 17 is the bright Seyfert galaxy discussed by Willner et al. (2023, their Figure 3). XMM 86 was not covered by JWST.

liabilities of all the candidate counterparts and the total number of sources with $LR > LR_{th}$. The completeness (C) of the sample is defined as the ratio between the sum of the reliability of all the candidate counterparts and the number of the X-ray sources that have ancillary objects within the search radius.

A higher LR_{th} suggests a higher reliability of the matching but lower sample completeness, while a lower LR_{th} suggests a lower reliability of the matching but higher sample completeness. We selected LR_{th} following Brusa et al. (2007) by maximizing $(R + C)/2$. We applied this criterion to the five ancillary catalogs (HSC, J-PAS, SDSS, MMIRS, WISE) and the resulting LR_{th} are 0.3, 0.2, 0.2, 0.3, and 0.1, respectively. The corresponding numbers of the XMM-Newton sources that have at least one counterpart above the chosen LR_{th} are given in Table 8. We used the HSC catalog as the primary reference for visible-wavelength counterparts because it is the deepest and covers the most area. Similarly, we used the MMIRS catalog as the primary for the infrared counterparts. Other catalogs were checked if no counterpart was found in the primary catalog.

The identified counterparts of XMM-Newton sources can be separated into three classes:

- **Secure:** these are sources with a single counterpart with $LR > LR_{th}$, or it has more than one candidate counterpart but the LR of the primary counterpart is four times higher than the LR of the secondary counterpart. (For there to be more than one candidate, both primary and secondary counterparts must have $LR > LR_{th}$).
- **Ambiguous:** these are sources with multiple candidate counterparts with the LR of the primary counterpart being less than four times higher than the LR of the secondary counterpart or the secure optical counterpart being different from the IR counterpart.
- **Unidentified:** these are sources with no optical or IR counterpart with $LR > LR_{th}$ within the search radius.

The NEP-TDF also has Chandra coverage, which provides better localization of some of the X-ray sources. Therefore, we utilized the Chandra NEP-TDF source catalog (Maksym et al., in prep.) to help identify the ancillary counterparts of the XMM-Newton sources with ambiguous counterparts. In ambiguous cases, we selected the ancillary counterpart that is closer to the Chandra measured position (which is also the primary counterpart of the XMM-Newton source in most cases) as the secure ancillary counterpart of the XMM-Newton

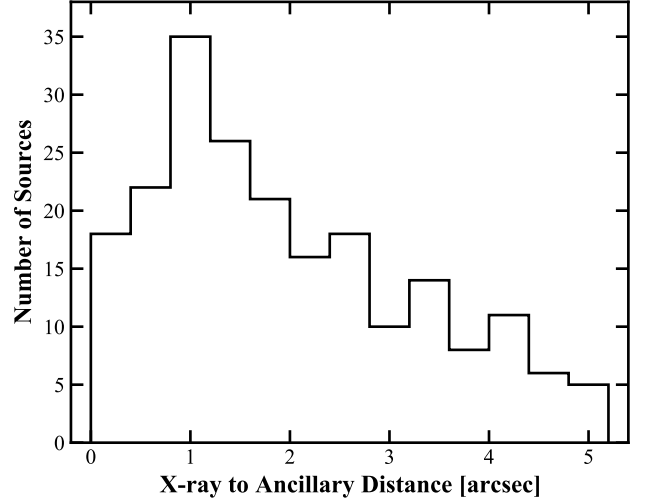


Figure 15. Distribution of separations between XMM-Newton sources and their secure ancillary counterparts. The median separation is $1''.69$.

source. We also visually inspected all identifications on the XMM-Newton, HSC, and MMIRS images. Figure 14 shows three XMM-Newton sources with secure, ambiguous, and unidentified ancillary counterparts.

The source XMM ID 17 (=NuSTAR ID 58 = J172241+6542.6, $z = 0.1791$) shown in Figure 14 is a heavily obscured Seyfert galaxy with column density $N_H \sim 10^{23} \text{ cm}^{-2}$ measured by NuSTAR and $N_H \geq 10^{23} \text{ cm}^{-2}$ by XMM-Newton. (See Section 7.2 for more discussion.) This heavily obscured scenario is also supported by the JWST and HST imaging. The strong red spikes seen on the JWST images suggest that the nucleus is a dusty point source. The clear host-galaxy feature in yellow shown on the HST image also implies a significantly obscured core.

A total of 214 XMM-Newton sources have secure ancillary counterparts. 19 XMM-Newton sources have ambiguous ancillary counterparts, out of which 14, 3, 1, and 1 have two, three, four, and five candidate ancillary counterparts within the search radius and with $LR > LR_{th}$. The coordinates and fluxes of the optical and IR counterparts of the XMM-Newton sources are listed in Tables 9 and 10. The distribution of the separations between XMM-Newton sources and their secure ancillary counterparts is shown in Figure 15; the median separation is $1''.69$.

6.4. Radio Counterparts

The NEP-TDF was observed in the radio “S band” ($\nu = 3 \text{ GHz}$) by the Karl G. Jansky Very Large Array (VLA; PIs: R. A. Windhorst & W. Cotton). The 48-hour VLA survey (Hyun et al. 2023) covered an area of $\sim 0.126 \text{ deg}^2$ ($24'$ in diameter), centered at the

bright (in both radio and X-ray) blazar (NuSTAR ID 29, $z = 1.441$). Therefore, only about 55% of the XMM-Newton area was covered by VLA. The Hyun et al. (2023) source list comprises 756 sources at $S/N > 5$. The 1σ noise is $1\mu\text{Jy beam}^{-1}$ at the primary-beam center. As the angular resolution is FWHM $0''.7$, we matched the VLA catalog with the ancillary counterparts of the XMM-Newton-detected sources using $0''.7$ as the matching radius and did not consider the unidentified sources. With this procedure, 55 out of the 171 XMM-Newton sources covered by the VLA have VLA counterparts. This fraction is consistent with what was discovered in COSMOS, where $\sim 40\%$ of the X-ray sources have VLA counterparts (Smolčić et al. 2017; Marchesi et al. 2016). The radio-brightest source in the XMM-Newton sample is the blazar (NuSTAR ID 29) with a 3 GHz flux of 0.2 Jy. The median flux of the XMM-Newton matched VLA sample is $23\mu\text{Jy}$. Both the NuSTAR and XMM-Newton catalogs report the VLA ID and fluxes from Hyun et al. (2023).

Willner et al. (2023) reported the 62 VLA sources that have JWST counterparts. Six sources were detected by XMM-Newton (ID 17/29/49/65/179/197). Hyun et al. (2023) also reported the James Clerk Maxwell Telescope (JCMT) SCUBA-2 850 μm survey of the JWST NEP-TDF with 114 sources detected at $S/N > 3.5$. Four XMM-Newton sources (ID 1/42/70/91) have JCMT counterparts.

6.5. HST and JWST counterparts

HST observations of the JWST NEP-TDF (GO15278, PI: R. Jansen and GO16252/16793, PIs: R. Jansen & N. Grogin) were taken between 2020 September 25 and 2022 October 31. These observations include imaging with WFC3/UVIS in the F275W (272 nm) filter and with ACS/WFC in the F435W (433 nm) and F606W (592 nm) filters (O’Brien et al. 2024, R. A. Jansen et al., in prep.). The 2σ limiting depths are $\text{mag}_{\text{AB}} \simeq 28.0, 28.6, \text{ and } 29.5$ mag in F275W, F435W, and F606W, respectively, and the ACS/WFC observations cover a total area of $\sim 194\text{ arcmin}^2$.

The JWST observations of the NEP-TDF (PI: R. A. Windhorst & H. B. Hammel, PID 2738) were taken in four epochs between 2022 August 26 and 2023 May 21 (Windhorst et al. 2023). The survey includes eight NIRCcam filters with 5σ point-source AB limits for each epoch of observation $\simeq 28.6, 28.8, 28.9, 29.1, 28.8, 28.8, 28.1, \text{ and } 28.3$ mag in F090W, F115W, F150W, F200W, F277W, F356W, F410W, and F444W, respectively. Each NIRCcam epoch of observation covers an area of $2'.15 \times 6'.36$ with the four epochs together (Figure 10) covering $\sim 55\text{ arcmin}^2$. The survey also includes

NIRISS grism data with 1σ continuum sensitivity 25.9. Each NIRISS epoch covers an area of $2'.22 \times 4'.90$.

The HST and JWST NEP-TDF surveys are much deeper than the HSC and MMIRS/WISE catalogs, but they cover only the center 26% and 7% of the XMM-Newton survey area, respectively. Therefore, we did not use the HST and JWST catalogs to identify the multi-wavelength counterparts of the XMM-Newton sources. Instead we used the coordinates of the counterparts of the XMM-Newton sources (Section 6.3) to match the HST (Jansen et al., in prep) and JWST catalogs (Windhorst et al. 2023, Windhorst et al., in prep). We used the F606W HST catalog and F444W JWST catalog when matching, as they have the deepest sensitivities. In all, 102 XMM-Newton sources have HST counterparts, and 32 XMM-Newton sources have JWST counterparts. The NuSTAR and XMM-Newton catalogs report the F606W and F444W fluxes.

6.6. Redshifts

Some of the NEP-TDF X-ray sources have redshifts measured from optical spectra. Spectra came from Hectospec⁹ (Fabricant et al. 2005) and Binospec¹⁰ (Fabricant et al. 2019), both of which are mounted on the 6.5 m MMT.

Hectospec is multi-object spectrograph with 300 optical fibers. Its 1° -diameter field of view makes it an efficient instrument to survey the NEP-TDF X-ray sources because of their relatively low areal density. Therefore, we observed (PI: Zhao) the XMM-Newton-selected sources with Hectospec on 2022 Sep 1 and with a different fiber configuration on 2023 May 20. Each exposure was 2 hours split into six 1200 s exposures to avoid saturation of bright targets, remove cosmic rays, and improve pipeline reduction. The 270 line mm^{-1} grating provided spectral resolution $R \sim 1000\text{--}2000$ over the wavelength range 3800–9200 Å, and each exposure allows measuring redshifts of sources with $m_i \leq 22\text{ AB}$. A limitation of Hectospec is that adjacent fibers cannot be placed within $20''$ of each other. In all, we obtained 41 spectra with good enough S/N to measure the redshifts of XMM-Newton targets in the 2022 run and 37 spectra in the 2023 run. Those include spectra of both possible counterparts of XMM-Newton ID 187. Besides the XMM-Newton targets, we also observed 40 ($i \leq 21\text{ mag}$) targets selected from the VLA (Hyun et al. 2023) and Chandra-detected (Maksym et al., in prep) sources. Table 11 in Appendix APPENDIX C reports their redshifts and spectral types.

⁹ <https://lweb.cfa.harvard.edu/mmti/hectospec.html>

¹⁰ <https://lweb.cfa.harvard.edu/mmti/binospec.html>

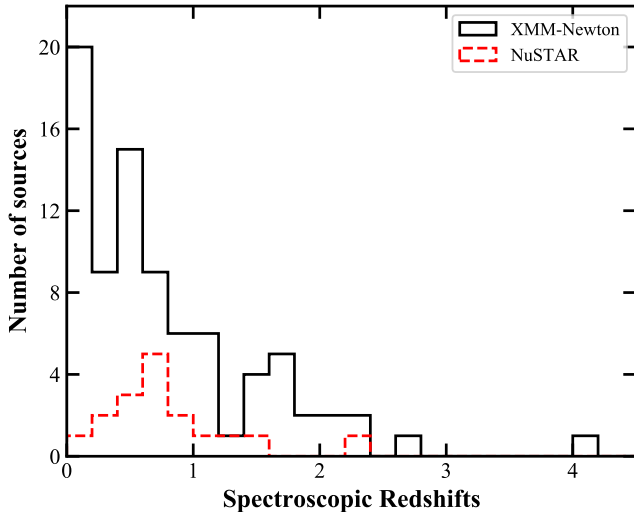


Figure 16. Spectroscopic redshifts of the XMM-Newton (black solid line) and NuSTAR (red dashed line) sources.

The Hectospec data were reduced using the IDL script HSRED¹¹ v2.0 (originally written by Richard Cool) developed by the Telescope Data Center at SAO (Mink et al. 2007). This pipeline provides fine-tuned wavelength calibrated, improved cosmic-ray rejected, and sky-subtracted 1D spectra. The redshifts were measured using a semi-automated and interactive Java toolkit, A Spectrum Eye Recognition Assistant¹² (ASERA; Yuan et al. 2013), which was developed to classify the spectra observed by the Large Sky Area Multi-object Fiber Spectroscopic Telescope (LAMOST; Wang et al. 1996). The spectroscopic redshifts were measured by cross-correlating the observed Hectospec spectra against a library of quasar, galaxy, and star template spectra¹³ from SDSS integrated into ASERA.

Binospec is an imaging spectrograph covering 3900–10,000 Å (Fabricant et al. 2019). C. N. A. Willmer obtained more than 1,378 optical spectra with Binospec and successfully measured more than 1,000 redshifts of the sources in NEP-TDF (Willmer et al., in prep). These include five additional XMM-Newton sources. Therefore, a total of 82 XMM-Newton sources have spectroscopic redshifts. We categorized the sources into quasars (presenting broad emission lines), galaxies (including Type 2 AGN, which have only narrow emission lines), and stars. Future efforts to identify type 2 AGN can include methods such as the BPT diagram (e.g., Kewley et al. 2001; Kauffmann et al. 2003).

¹¹ <http://www.mmt.org/hsred-reduction-pipeline/>

¹² https://gitee.com/yuanhl1984/asera_pub/

¹³ <http://www.sdss.org/dr5/algorithms/spectemplates/>

Photometric redshifts of the X-ray source counterparts were adopted from the SDSS DR17 catalog (Abdurro’uf et al. 2022). Only photometric redshifts with low root-mean-square (RMS) uncertainties, specifically the `photoErrorClass` flag = −1, 1, 2, or 3 were considered. That added two XMM-Newton sources without spectroscopic redshifts for a total of 84 XMM-Newton sources with redshifts, reported in Tables 9 and 10.

6.7. X-ray to Optical Properties

The X-ray to optical flux (X/O) ratio has been historically used to identify the nature of X-ray sources (e.g., Maccacaro et al. 1988). The ratio is defined as:

$$X/O \equiv \log(f_X/f_{\text{opt}}) = \log(f_X) + m_{\text{opt}}/2.5 + C \quad (5)$$

where f_X is the X-ray flux in a given band in units of $\text{erg cm}^{-2} \text{s}^{-1}$, m_{opt} is the optical AB magnitude in a given filter, and C is a constant depending on the bands chosen in X-ray and optical. Figure 17 shows the i -band (HSC) magnitudes as a function of the soft (0.5–2 keV) and hard (2–10 keV) X-ray fluxes of the XMM-Newton-detected sources. The constants used to calculate X/O are $C_{0.5-2} = 5.91$ and $C_{2-10} = 5.44$ for the soft and hard bands, respectively (Marchesi et al. 2016).

The majority of X-ray (both XMM-Newton and NuSTAR) detected sources are AGN with $-1 < X/O < 1$, as found in previous surveys (e.g., Stocke et al. 1991; Schmidt et al. 1998; Akiyama et al. 2000; Marchesi et al. 2016). Previous Chandra and XMM-Newton surveys (Hornschemeier et al. 2001; Fiore et al. 2003; Civano et al. 2005; Brusa et al. 2007; Laird et al. 2008; Xue et al. 2011) and NuSTAR surveys (Civano et al. 2015; Lansbury et al. 2017) detected sources having $X/O > 1$. These sources were associated with high redshifts or large obscurations. Some sources with $X/O < -1$ are stars, as shown in Figure 17. Many galaxies are in the AGN locus. Most of these sources are likely to be type 2 AGN rather than quiescent or star-forming galaxies because their 2–10 keV luminosities (Figure 18) are mostly $>10^{42} \text{ erg s}^{-1}$ (the conventional threshold when separating AGN from galaxies; e.g., Basu-Zych et al. 2013). Furthermore, only about five galaxies are expected in the FoV considering the galaxy number density (Ranalli et al. 2005; Luo et al. 2017; Marchesi et al. 2020).

6.8. Luminosity–Redshift Distribution

Figure 18 shows the 0.5–2 keV and 2–10 keV rest-frame luminosities of the 85 XMM-Newton sources as a function of redshift. The rest-frame luminosities were calculated by converting their observed 0.5–2 keV and 2–10 keV fluxes with a K-correction assuming X-ray spectral indices $\Gamma(0.5-2 \text{ keV}) = 1.40$ and $\Gamma(2-10 \text{ keV}) =$

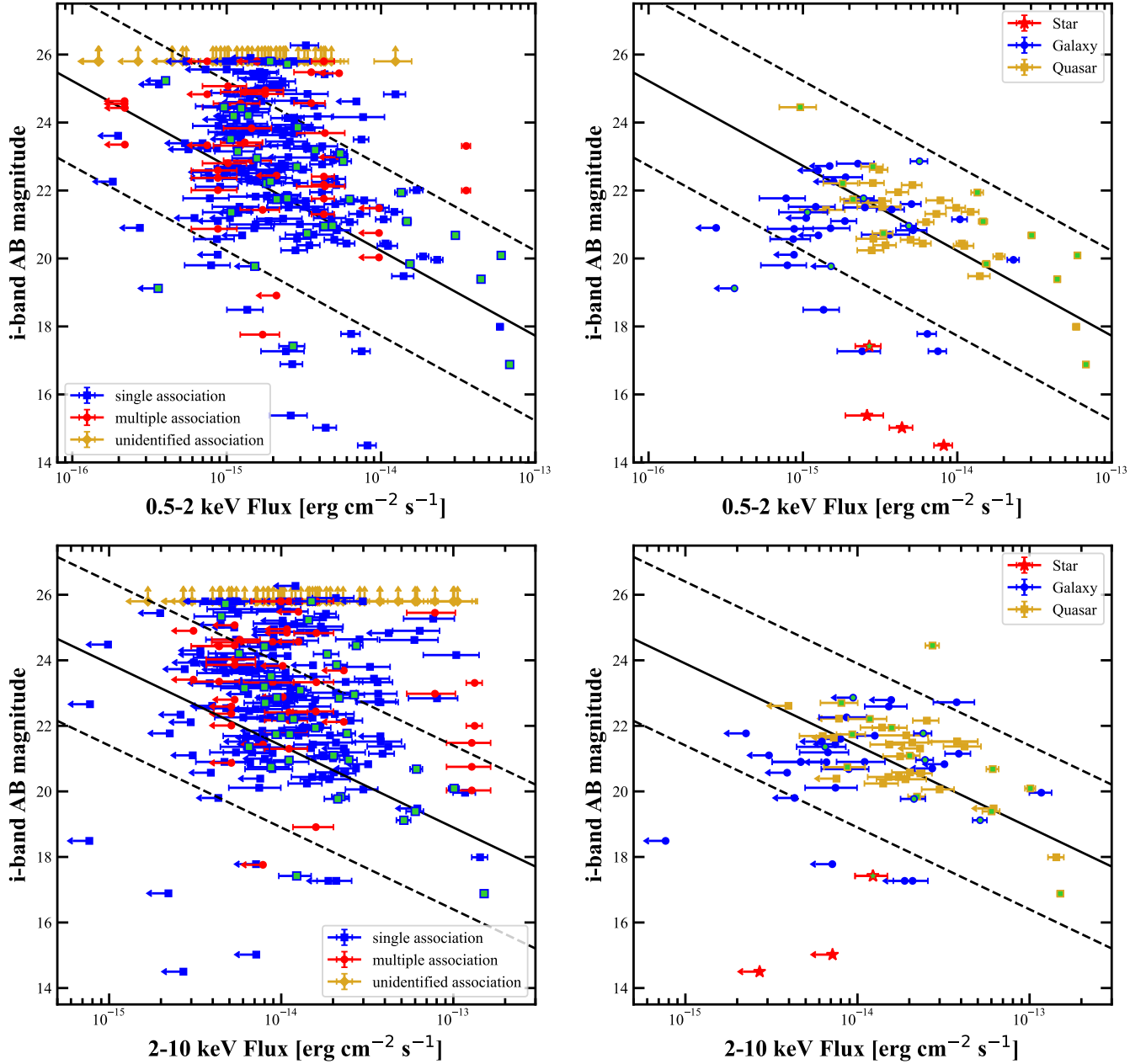


Figure 17. The *i*-band magnitudes of XMM-Newton counterparts as a function of X-ray fluxes. XMM-Newton sources with NuSTAR counterparts are plotted as open symbols filled with green. The solid and dashed lines represent the classical AGN locus, $X/O = 0 \pm 1$ (Maccacaro et al. 1988). Upper panels show the distribution of sources in soft X-rays and lower panels those in hard X-rays. The left panels show the entire sample of XMM-Newton sources. Symbols identify sources that have single, multiple, or no candidate counterparts as indicated in the legend. For the 18 XMM-Newton sources with ambiguous optical counterparts, all candidate optical counterparts are plotted. The 66 XMM-Newton sources without optical counterparts are plotted with 3σ upper limits $m_i > 25.8$. The right panels show only sources that have secure counterparts with spectroscopic identifications. Symbols indicate the type of source.

1.80. The calculated luminosities were not corrected for absorption, although the absorbing effect is partly mitigated by the choice of $\Gamma = 1.40$ in the 0.5–2 keV band.

Figure 19 shows the 10–40 keV rest-frame luminosities of the 22 NuSTAR sources that have redshift measurements. The 10–40 keV rest-frame luminosities were calculated by converting the observed 3–24 keV fluxes with a K-correction assuming $\Gamma = 1.80$. The brightest source in the FoV is a flat-spectrum radio quasar (FSRQ) blazar (ID 29, $z = 1.441$). Figure 19 also shows sources detected in previous NuSTAR surveys. Most of the detected sources from previous NuSTAR extragalactic surveys are well above the NEP-TDF sensitivity line, consistent with the NuSTAR survey being the deepest. The all-sky Swift-BAT survey is also shown in Figure 19. Its measured 14–195 keV luminosities (Gehrels et al. 2004; Barthelmy et al. 2005) from the 105-month Swift-BAT catalog (Oh et al. 2018) were converted to 10–40 keV luminosities (assuming a $\Gamma = 1.8$ power law model) for plotting. Swift-BAT samples sources mostly in the local Universe with median redshift of $\langle z_{\text{BAT}} \rangle = 0.044$, while NuSTAR samples sources at $\langle z_{\text{NuS}} \rangle = 0.734$.

7. DISCUSSION

7.1. $\log N$ – $\log S$

The cumulative hard X-ray source number-counts distributions ($\log N$ – $\log S$) in three energy bands (3–8 keV, 8–24 keV, and 8–16 keV) were calculated using the NEP-TDF cycle 5 (681 ks) observations Z21. Here, we update the $\log N$ – $\log S$ distributions by using the combined cycles 5+6 (1.56 Ms) data, which can provide constraints of $\log N$ – $\log S$ at fainter hard X-ray fluxes.

The $\log N$ – $\log S$ distribution is defined following Cappelluti et al. (2009) as:

$$N(>S) \equiv \sum_{i=1}^{N_S} \frac{1}{\Omega_i} \text{ deg}^{-2} \quad , \quad (6)$$

where $N(>S)$ is the surface density of sources detected above 95% reliability level in a given energy band with flux greater than S , and Ω_i is the sky coverage associated with the flux of the i th source (Figure 5). The variance of $N(>S)$ is

$$\sigma_S^2 = \sum_{i=1}^{N_S} \left(\frac{1}{\Omega_i} \right)^2 \quad . \quad (7)$$

The $\log N$ – $\log S$ distribution depends on the minimum flux limit and the S/N limit of the sources (Cappelluti et al. 2009; Puccetti et al. 2009). We selected a flux limit equal to 1/3 of the flux corresponding to the half-area coverage sensitivity reported in Table 6 in each band

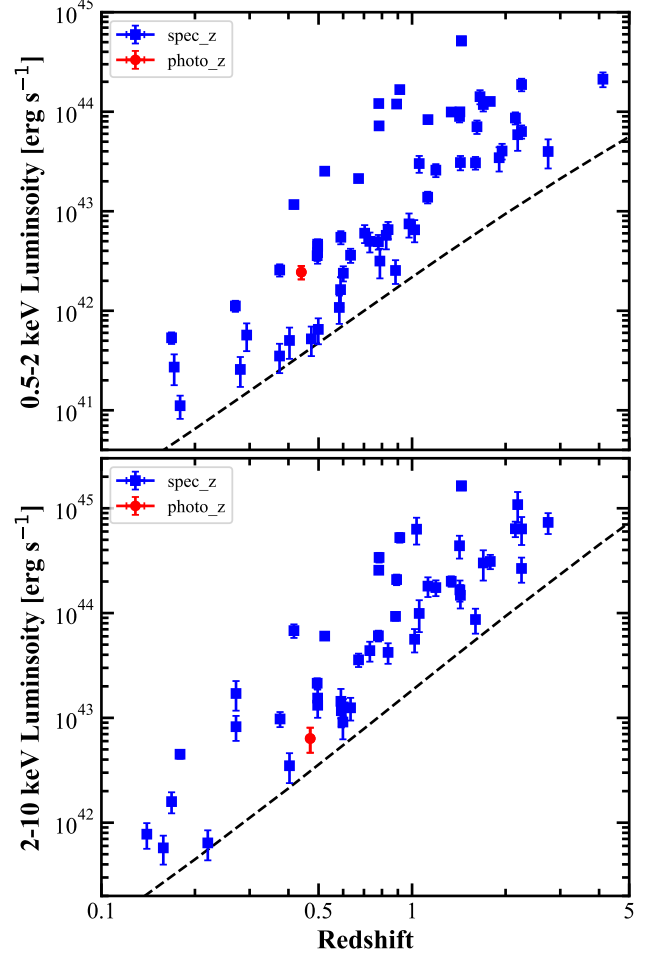


Figure 18. X-ray rest-frame luminosity versus redshift for the 84 XMM-Newton NEP-TDF sources with redshifts. The upper panel shows soft X-rays, and the lower panel shows hard X-rays. X-ray luminosities are as observed, not corrected for absorption. Sources with spectroscopic redshifts are plotted using blue squares, and a source with only a photometric redshift is plotted as a red circle. The 20%-area sensitivities are plotted as black dashed lines.

(Masini et al. 2018a, Z21). This reduces the effect of Eddington bias (Figure 8). To reduce the large uncertainties in the flux of low-S/N sources (Appendix APPENDIX A and Figure 24), we kept only sources detected with $S/N > 2.5$ (following Puccetti et al. 2009). Here S/N is defined as $C_{\text{net}}/(C_{\text{tot}} + C_{\text{bk}})^{0.5}$, where C_{net} is the source net counts, C_{tot} is the total counts, and C_{bk} is the background counts. For the maximum flux, we adopted $10^{-13} \text{ erg cm}^{-2} \text{ s}^{-1}$ for the 3–8 keV and 8–24 keV bands and $6 \times 10^{-14} \text{ erg cm}^{-2} \text{ s}^{-1}$ for the 8–16 keV band to provide enough statistics at the high-flux end.

To validate the selection of the minimum flux limit and the S/N limit, we calculated the $\log N$ – $\log S$ distributions in different energy bands using the selected minimum flux limits and the S/N limit from the 2400 simu-

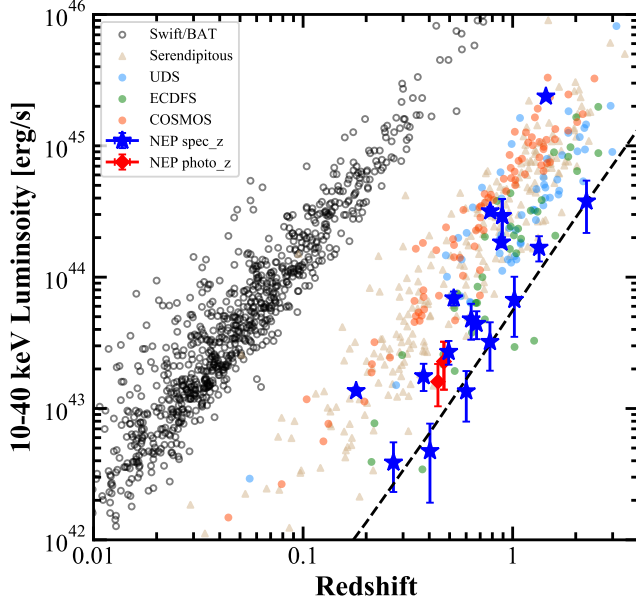


Figure 19. 10–40 keV rest-frame luminosity versus redshift for the NuSTAR sources with redshifts. Sources with spectroscopic (photometric) redshifts are plotted as blue stars (red diamonds). The sensitivity of the NEP-TDF cycles 5+6 survey at 20% sky coverage is plotted as a dashed line. NuSTAR COSMOS (red circles; [Civano et al. 2015](#)), ECDFS (green circles; [Mullaney et al. 2015](#)), UDS (blue circles; [Masini et al. 2018a](#)), 40-month serendipitous (brown triangles; [Lansbury et al. 2017](#)), and Swift-BAT 105-month (black open circles; [Oh et al. 2018](#)) surveys are shown as well. The luminosities were not corrected for intrinsic absorption.

lations described in Section 2.4. The calculated $\log N$ – $\log S$ distributions reproduce the input $\log N$ – $\log S$ distribution ([Treister et al. 2009](#)) in the simulations, suggesting the selected minimum flux limits and the S/N limits are reasonable for the real observations. Other choices of minimum flux (e.g., 20%–area sensitivity) and S/N limits (e.g., $S/N_{\text{lim}} = 2$ or $S/N_{\text{lim}} = 3$) were unable to reproduce the input $\log N$ – $\log S$ distribution. A minimum flux limit at 20%–area sensitivity leads to an $\sim 30\%$ over-estimation of $N(>S)$ at the faint end, $S/N_{\text{lim}} = 2$ leads to an over-estimation of $N(>S)$ by $\sim 35\%$, and $S/N_{\text{lim}} = 3$ leads to an under-estimate of $N(>S)$ by $\sim 40\%$ at the faint end.

Figure 20 shows the calculated $\log N$ – $\log S$ distributions from the actual cycle 5+6 observations. The NEP-TDF survey reaches fainter 8–24 keV fluxes than previous NuSTAR extragalactic surveys (i.e., COSMOS, EGS, and ECDFS; [Harrison et al. 2016](#)). The number of sources at the bright end in the 3–8 keV and 8–24 keV bands is a little high but (at $\sim 1\sigma$) consistent with previous measurements, especially given cosmic variance in the $\sim 0.16 \text{ deg}^2$ area of the NEP-TDF survey. This ex-

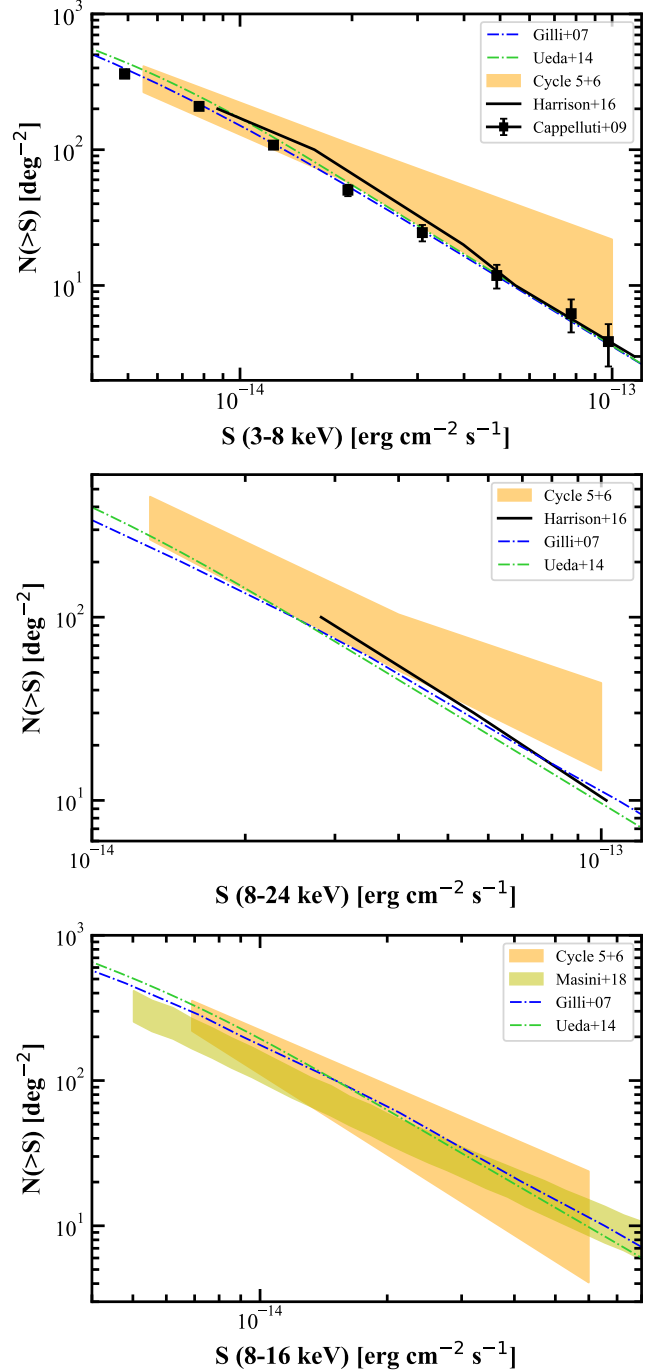


Figure 20. Cumulative source number counts as a function of X-ray flux. Panels show three energy ranges as labeled. The orange-shaded areas represents the 68%-confidence region at each energy. Black solid lines show results from [Harrison et al. \(2016\)](#), and yellow shaded areas show those of [Masini et al. \(2018b\)](#) using NuSTAR. Black points in the top panel show XMM-Newton results from [Cappelluti et al. \(2009\)](#). Expectations from population-synthesis models ([Gilli et al. 2007](#); [Ueda et al. 2014](#)) are shown by dot-dash lines as indicated in the legend.

cess cannot be explained solely by the bright blazar in the FoV. The observed $\log N$ – $\log S$ distributions are also generally consistent with CXB population-synthesis models (e.g., [Gilli et al. 2007](#); [Ueda et al. 2014](#)). However, there may be an excess of hard X-ray sources at the faint end of the 8–24 keV distribution, although again only at the $\sim 1\sigma$ level. Extrapolating the [Harrison et al. \(2016\)](#) $\log N$ – $\log S$ distribution shows a possible excess, but [Masini et al. \(2018a\)](#) found no such excess at 8–16 keV in the UDS field. If this excess is real, more heavily obscured sources exist than predicted by the population-synthesis models.

7.2. Hardness Ratio

Hardness ratio (HR) is useful to characterize the spectral shape of the XMM-Newton and NuSTAR NEP-TDF sources. The HRs of different column densities were estimated using a physical model which is typically used for modeling AGN X-ray spectra. The model includes a line-of-sight component (modeled by an absorbed power law), reflection component (modeled by `borus02`, [Baloković et al. 2018](#)), and scattered emission of soft X-rays (modeled by a fractional power law). The model was calculated with XSPEC as `phabs*(zphabs*powerlw+borus+constant*powerlw)`. `phabs` models the Galactic absorption. We assumed a photon index $\Gamma = 1.8$ in both `powerlw` and `borus02` and a torus column density $N_{\text{H,Tor}} = 1.4 \times 10^{24} \text{ cm}^{-2}$, a covering factor of $f_c = 0.67$ in `borus02`, and an inclination angle $\theta_{\text{inc}} = 60^\circ$ following the torus properties measured by [Zhao et al. \(2021b\)](#). We assumed a `constant` = 1% fraction of the intrinsic emission being scattered ([Ricci et al. 2017](#)).

Table 10 reports the HRs of XMM-Newton sources. They are defined as $(H - S)/(H + S)$ with 0.5–2 keV flux as the soft band flux S and 2–10 keV flux as the hard band flux H . Table 10 also reports S and H , which were calculated with the SAS `emldetect` tool. Figure 21 shows the HR distribution of the 286 XMM-Newton sources. The expected HR for a given obscuration depends on the source redshift as shown in Figure 21. About half (48%) of the XMM-Newton-detected sources have HR larger than expected for column density $N_{\text{H}} = 10^{22} \text{ cm}^{-2}$ or have a lower limit of HR that implies an obscured source. For the 85 XMM-Newton sources that have redshift measurements, 38% are obscured. That lower percentage might be due to the bias from $m_i \leq 22$ mag selection for Hectospec observation: obscured sources are typically fainter in the visible light than unobscured ones.

The HRs of the NuSTAR sources detected in the cycles 5+6 survey were calculated using a Bayesian

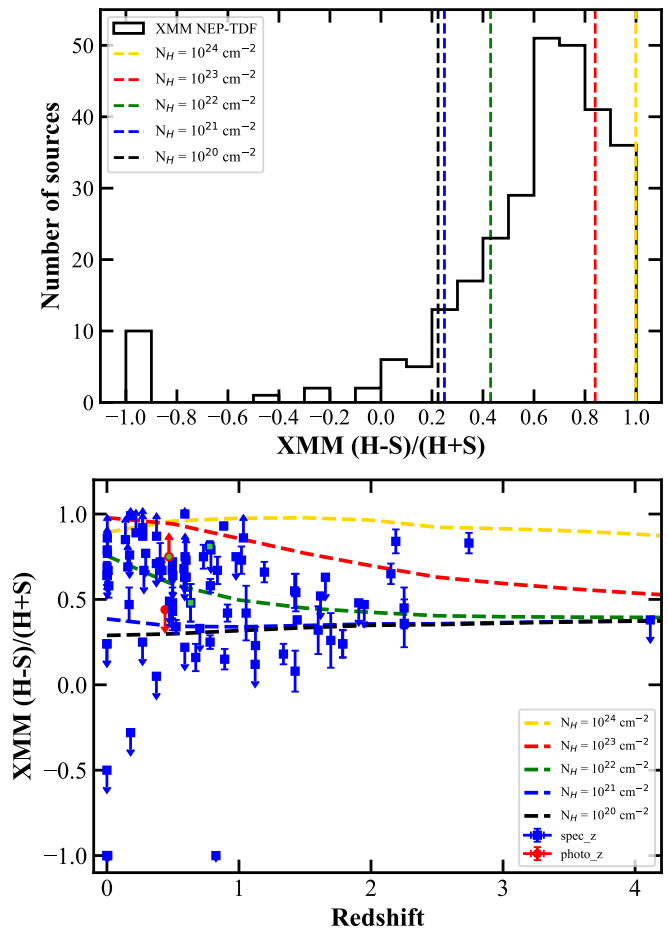


Figure 21. Top: $\log(\text{HR})$ distribution of the 286 XMM-Newton-detected sources. Dashed lines show the expected $\log(\text{HR})$ for a source at $z = 0.60$ (the mean redshift of the XMM-Newton sources with spectroscopic redshifts) and different obscuring column densities N_{H} as labeled. Bottom: $\log(\text{HR})$ of XMM-Newton sources versus redshift. Blue squares represent sources with spectroscopic redshifts and red circles those with photometric redshifts. Dashed lines show the expected HR N_{H} for different column densities as labeled. The three CT-AGN candidates detected by NuSTAR (Figure 22) are shown as green-filled symbols.

method (BEHR; [Park et al. 2006](#)) following [Z21](#). BEHR can estimate HR even for sources in the Poisson regime with a limited number of counts. BEHR also calculates the mode and uncertainty of the HR distribution of each source based on the source’s total and background counts. Here, S and H were defined as net counts in the 3–8 keV and 8–24 keV bands, respectively. The 1σ uncertainty was calculated by Gaussian-quadrature numerical integration when the number of the net counts of either energy band was less than 15 or by the Gibbs sampler method when the number of net counts was larger. The differences in the effective exposure times between the two bands were considered. The upper panel of Fig-

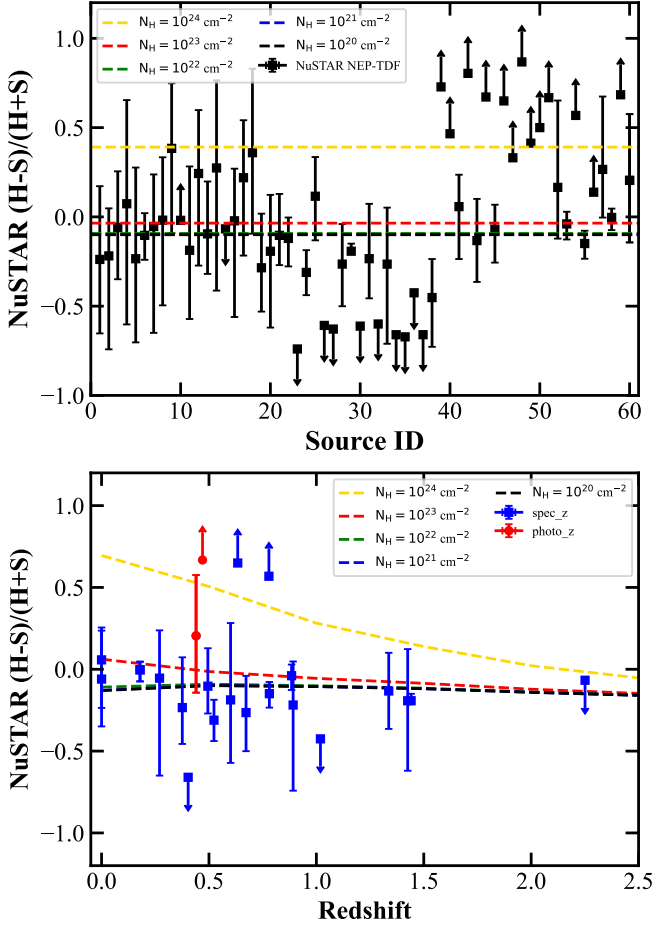


Figure 22. Top: $\log(\text{HR})$ distribution of all 60 NuSTAR-detected sources versus source ID. Dashed lines show expected HRs for $z = 0.734$, the median redshift of the NuSTAR sources having measured redshifts, and for values of N_{H} as labeled. Bottom: $\log(\text{HR})$ of NuSTAR sources with spectroscopic (blue square) or photometric (red circle) redshifts as a function of their redshifts. Dashed lines are the expected HR for different N_{H} values as labeled. (The green, blue, and black lines overlap.)

ure 22 shows the HR of the 60 NuSTAR sources. We converted the soft and hard band fluxes to count rate using the CF listed in Section 3.1 when calculating the model predicted HR to directly compare with the BEHR calculated HR.

Unlike XMM-Newton, NuSTAR is sensitive to obscurations $N_{\text{H}} > 10^{23} \text{ cm}^{-2}$ (e.g., Masini et al. 2018a). 47% of the NuSTAR detected sources are obscured above that level, and 23% are Compton-thick (CT, $N_{\text{H}} > 10^{24} \text{ cm}^{-2}$) assuming $z = 0.734$ (median redshift of the NuSTAR sources). CT candidates include sources that have lower limits on their HR. Figure 22 shows HR as a function of redshift for the 22 NuSTAR sources with

redshift measurements. Of these, 23% are heavily obscured, and 14% are CT.

The HRs of the XMM-Newton sources and the model predictions used to compare with the NuSTAR HRs were calculated assuming particular spectral shapes when converting the count rates into fluxes. Different assumed column densities and photon indices lead to different ECFs. The ECF changes by about 70% in the 0.5–2 keV band and about 20% in the 8–24 keV band assuming no intrinsic absorption compared to a CT absorption. This might explain the discrepancy of the column densities estimated using NuSTAR and XMM-Newton. Changing the photon index has little effect: only $\sim 5\%$ for photon indices $\Gamma = 1.40$ or 2.20 rather than the assumed $\Gamma = 1.80$. Therefore, a broadband spectral analysis is needed to accurately measure the obscuration of these sources. Full spectral analysis of the NuSTAR and XMM-Newton sources will be presented by S. Creech et al. in prep.

7.3. CT Fraction

As shown in Section 7.2, XMM-Newton is more sensitive to distinguishing between obscured and unobscured sources, while NuSTAR is more powerful in determining whether a source is CT. Three CT sources (ID 46/51/54) with redshift measurements are shown in Figure 22. Three additional sources (ID 39/42/48) lack redshift measurements but have $\text{HR} > 0.736$, the CT threshold at $z = 0$. Therefore, at least six sources are CT based on HR. For the rest of the sources without redshift measurements, five are CT candidates if $z \geq 0.734$. Another 12 sources have HR uncertainty ranges that include the $z = 0.734$ CT threshold. A reasonable estimate is that $(3 + 3 + 5)/60 = 18\%$ of sources are CT with limits of 6–23 sources or 10–38%. Additional redshift measurements are needed to tighten the constraints on the CT fraction.

The CT fraction measured in the NEP field is consistent with the CT fraction measured in other surveys as shown in Figure 23. The most directly comparable values are for the NuSTAR COSMOS field ($13\% - 20\%$; Civano et al. 2015) and the NuSTAR UDS field ($11.5\% \pm 2.0\%$; Masini et al. 2018a). For the Swift-BAT all-sky survey, which samples the bright end of the nearby AGN population, Burlon et al. (2011) and Ricci et al. (2015) measured a CT fraction of $\sim 4.6\% - 7.6\%$. However, a recent analysis (Torres-Albà et al. 2021) of the CT-AGN candidates in the BAT sample using high-quality NuSTAR observations found that many candidates are less than CT-obscured. That brought the CT fraction of the entire BAT sample down to $3.5\% \pm 0.5\%$. However, Torres-Albà et al. (2021) also found that the

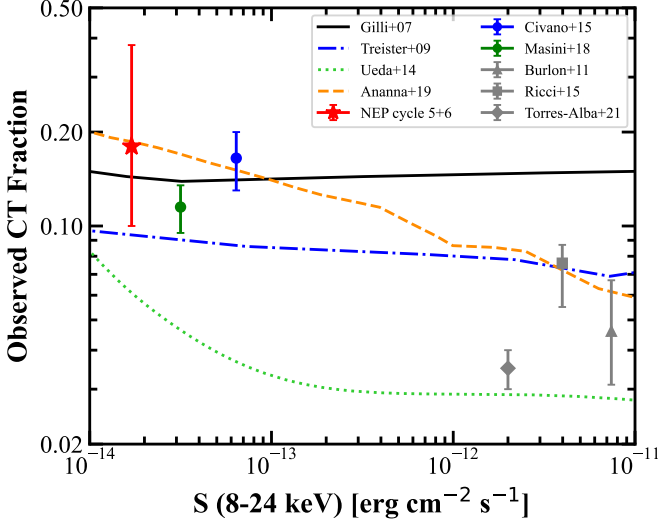


Figure 23. CT fraction in different surveys as a function of survey sensitivity limit. The CT fraction measured here is plotted as a red star. Blue and green circles represent the NuSTAR measurements in the COSMOS (Civano et al. 2015) and UDS (Masini et al. 2018a) fields. The grey triangle, square, and diamond show the Swift-BAT measurements (Burlon et al. 2011; Ricci et al. 2015; Torres-Albà et al. 2021). Lines show the CT fractions predicted by CXB synthesis models: Gilli et al. (2007) (black solid line), Treister et al. (2009) (blue dash-dot line), Ueda et al. (2014) (green dot line), and Ananna et al. (2019) (orange dashed line).

CT fraction of the BAT sample depends on the redshift range. A CT fraction of 20% was found for the $z \leq 0.01$ sample and 8% for $z \leq 0.05$ sample. This discrepancy was explained by BAT being biased against the detection of CT sources at higher redshift. Figure 23 compares the measured CT fractions with population-synthesis model predictions (Gilli et al. 2007; Treister et al. 2009; Ueda et al. 2014; Ananna et al. 2019). The recent Ananna et al. (2019) model is in good agreement with the hard X-ray observed CT-AGN fraction at both bright and faint fluxes.

7.4. An obscured and variable Seyfert galaxy

In addition to the bright blazar mentioned in Section 6.8, there is another prominent Seyfert galaxy (and radio source; Willner et al. 2023) in the TDF field. The source XMM ID 17 (shown in Figure 14, NuSTAR ID 58) has XMM-Newton $\text{HR} \geq 0.99$ suggesting $N_{\text{H}} > 10^{23} \text{ cm}^{-2}$ (Figure 21). The NuSTAR $\text{HR} = 0.00^{+0.05}_{-0.07}$ also suggests $N_{\text{H}} \sim 10^{23} \text{ cm}^{-2}$ (Figure 22). The bright core seen in the JWST long-wave imaging but not at shorter wavelengths supports the interpretation of high but not CT obscuration. The source’s 2–10 keV luminosity $L(2\text{--}10 \text{ keV}) = 4.5 \pm 0.5 \times 10^{42} \text{ erg s}^{-1}$ and 10–40 keV luminosity $L(10\text{--}40 \text{ keV}) = 1.36 \pm 0.08 \times 10^{43}$

erg s^{-1} suggest a type 2 AGN. More intriguing, this source is variable at 3σ in 3–24 keV band and at 2.9σ in the 3–8 keV band but is not significantly variable in the 8–24 keV band, suggesting a variable spectral shape. Its count rates increased by 115% in the 3–24 keV and 230% in the 3–8 keV band from 2019 Oct to 2022 Jan (Figure 26). We did not find obvious variability of this source in either visible (Zwicky Transient Facility, ZTF; Bellm et al. 2019; Masci et al. 2019) or IR (NEOWISE; Mainzer et al. 2014). This suggests that the X-ray variability of the source might be caused by the decreasing of the line-of-sight obscuration rather than the variability of the intrinsic accretion rate. However, further investigation is needed.

8. CONCLUSIONS

The NuSTAR extragalactic survey of the JWST NEP-TDF attained a total of 1.5 Ms exposure and covered an area of $\sim 0.16 \text{ deg}^2$. This makes it the deepest NuSTAR extragalactic survey to date. The survey consists of 21 observations in NuSTAR cycles 5 and 6 across seven epochs from 2019 Sep to 2022 Jan, enabling a multi-year, multi-epoch study of this field in hard X-rays. Principal results are:

1. The NuSTAR cycle 6 survey was taken from Oct. 2020 to Jan. 2022 with a total exposure of 880 ks acquired in 12 observations over four epochs covering an area of $\sim 0.11 \text{ deg}^2$. A total of 35 sources were detected above the 95% reliability threshold in cycle 6. In the merged cycle 5 and 6 observations, which reach the deepest sensitivity, 60 sources were detected above the 95% reliability threshold.
2. The survey’s 8–24 keV sensitivities at 20%-area are $1.98 \times 10^{-14} \text{ erg cm}^{-2} \text{ s}^{-1}$ for NuSTAR cycle 6 and $1.70 \times 10^{-14} \text{ erg cm}^{-2} \text{ s}^{-1}$ for NuSTAR cycles 5+6. A $\sim 1\sigma$ excess of faint 8–24 keV sources compared to the population-synthesis models hints that more faint, heavily obscured sources might exist than predicted by the models.
3. To enable broadband (0.3–24 keV) X-ray spectral fitting and more reliable multiwavelength counterpart matching of the NuSTAR detected sources, a total of 60 ks XMM-Newton observations were taken simultaneously with NuSTAR in cycle 6. A total of 286 XMM-Newton sources were detected including more 3–8 keV sources at the bright end compared to previous number counts.
4. Of the 60 NuSTAR sources, 37 have XMM-Newton counterparts. Of the 23 NuSTAR sources without

XMM-Newton counterparts, 17 appear to be heavily obscured.

5. The NEP-TDF has extensive multiwavelength coverage, including Subaru/HSC, J-PAS, and SDSS in optical and MMT/MMIRS and WISE in IR. A total of 214 XMM-Newton sources have secure counterparts in multiwavelength catalogs, and 19 more have ambiguous counterparts. Deeper optical and IR observations covering the entire FoV of the XMM-Newton NEP-TDF survey are needed to identify counterparts of the remaining 53 XMM-Newton sources. In addition, VLA, HST, and JWST surveyed a fraction of the XMM-Newton NEP-TDF and a total of 55, 102, and 32 XMM-Newton sources have VLA, HST, and JWST counterparts, respectively.
6. Optical spectra of XMM-Newton counterparts produced 82 high-confidence redshifts. Two additional sources have photometric redshifts measured in SDSS DR17. The 84 XMM-Newton sources with redshifts include 22 NuSTAR sources. In addition, spectroscopic redshifts of 40 VLA and Chandra sources in the NEP-TDF are reported in Table 11.
7. Half (48%) of the XMM-Newton sources are obscured with $N_{\text{H}} > 10^{22} \text{ cm}^{-2}$, and 47% of the NuSTAR sources are heavily obscured with $N_{\text{H}} > 10^{23} \text{ cm}^{-2}$. $18^{+20}_{-10}\%$ of the NuSTAR sources are Compton-thick. Broadband spectral analysis is needed to accurately measure the column densities of the sources (S. Creech et al., in prep).
8. A type 2 AGN at $z = 0.1791$ has X-ray obscuration $N_{\text{H}} \sim 10^{23} \text{ cm}^{-2}$, and significant obscuration is supported by JWST and HST images. The source is significantly variable with its 3–8 keV band flux having increased by 230% in 26 months.
9. The prime goal of the NuSTAR NEP-TDF observations is to study hard X-ray variability. Preliminary results for the 60 sources detected in cycles 5+6 show four sources varying with $p < 0.05$ ($\sim 2\sigma$) in at least one energy band in the 26 months of observations. A detailed study of the source variability is in preparation.
10. Subsequent to the work reported here, an additional 855 ks of NuSTAR observations and 30 ks of XMM-Newton observations have been obtained in NuSTAR cycle 8 (PI: Civano, pid 8180, Silver et al., in prep.). These targeted the NEP-TDF simultaneously with JWST. A further 900 ks of

NuSTAR observations and 40 ks of XMM-Newton observations were approved for NuSTAR cycle 9 (PI: Civano, ID: 9267). Thus the NEP-TDF will acquire a total of 3.25 Ms NuSTAR observations, making it the newest and deepest NuSTAR extragalactic survey. The data will constitute five years of continuous hard X-ray monitoring of the field, making it the first long-term monitoring, contiguous survey of hard X-ray variability.

11. The rich multiwavelength coverage and multi-year NuSTAR monitoring of the NEP-TDF make it an ideal field for the next generation of hard X-ray surveys. The High-Energy X-ray Probe (HEX-P) concept¹⁴ (Madsen et al. 2019) has a larger effective area, much better PSF, and lower background compared with NuSTAR. This will allow ~ 20 times deeper sensitivity in the 8–24 keV band compared with the current deepest NuSTAR NEP-TDF survey and detect ~ 40 times more hard X-ray sources. HEX-P will be able to resolve more than 80% of the CXB into individual sources up to 40 keV (Civano et al. 2023) and better constrain current population-synthesis models. Its broadband coverage (0.2–80 keV) will allow X-ray spectral analysis of both obscured and unobscured sources and thus more accurately constrain the CT fraction down to $10^{-15} \text{ erg cm}^{-2} \text{ s}^{-1}$ (Civano et al. 2023; Boorman et al. 2023).

The authors thank the anonymous referee for their helpful comments. XZ acknowledges NASA funding under contract numbers 80NSSC20K0043 and 80NSSC22K0012. The authors thank Jinguo Liu for helping improve the code efficiency when calculating the variability of the NuSTAR and XMM-Newton sources, thereby shortening the calculation time by more than a factor of 10; Cheng Cheng for helping reduce the Hectospec spectra; Alberto Masini for help with the proposal preparation and for sharing the data of his previous papers; Nelson Caldwell and the MMT observing team for the help in generating the observing catalog and scheduling the Hectospec observations; Brian Grefenstette for helpful discussion of NuSTAR and its data analysis; Karl Foster and the NuSTAR observation planning team for their help in designing the observation plan and scheduling the observations.

This work has made use of data from the NuSTAR mission, a project led by the California Institute of

¹⁴ <https://hexp.org>

Technology, managed by the Jet Propulsion Laboratory, and funded by NASA. This research has made use of the NuSTAR Data Analysis Software (NuSTAR-DAS) jointly developed by the ASI Science Data Center (ASDC, Italy) and the California Institute of Technology (USA). This research made use of data and software provided by the High Energy Astrophysics Science Archive Research Center (HEASARC), which is a service of the Astrophysics Science Division at NASA/GSFC and the High Energy Astrophysics Division of the Smithsonian Astrophysical Observatory. This work is based on observations obtained with XMM-Newton, an ESA science mission with instruments and contributions directly funded by ESA Member States and NASA. The MMIRS, Hectospec, and Binospec observations reported were obtained at the MMT Observatory, a joint facility of the Smithsonian Institution and the University of Arizona. This paper uses data products produced by the OIR Telescope Data Center, supported by the Smithsonian Astrophysical Observa-

tory. This work makes use of the data from SDSS IV. Funding for the Sloan Digital Sky Survey IV has been provided by the Alfred P. Sloan Foundation, the U.S. Department of Energy Office of Science, and the Participating Institutions. This work is partly based on the data from WISE, which is a joint project of the University of California, Los Angeles, and the Jet Propulsion Laboratory/California Institute of Technology, and NEOWISE, which is a project of the Jet Propulsion Laboratory/California Institute of Technology.

Facilities: NuSTAR, XMM-Newton, Chandra, MMT (Binospec, Hectospec, and MMIRS), JWST, HST, Subaru/HSC, SDSS, J-PAS, WISE

DATA AVAILABILITY

Electronic versions of the generated NuSTAR and XMM-Newton catalogs as described in Appendix B can be found in Vizier at [link.tbd](#). (Link will be provided immediately after the paper is accepted.)

REFERENCES

- Abdurro'uf, Accetta, K., Aerts, C., et al. 2022, *ApJS*, 259, 35, doi: [10.3847/1538-4365/ac4414](#)
- Adams, N. J., Conselice, C. J., Austin, D., et al. 2023, arXiv e-prints, arXiv:2304.13721, doi: [10.48550/arXiv.2304.13721](#)
- Aihara, H., Arimoto, N., Armstrong, R., et al. 2018, *PASJ*, 70, S4, doi: [10.1093/pasj/psx066](#)
- Akiyama, M., Ohta, K., Yamada, T., et al. 2000, *The Astrophysical Journal*, 532, 700, doi: [10.1086/308606](#)
- Ananna, T. T., Treister, E., Urry, C. M., et al. 2019, *The Astrophysical Journal*, 871, 240, doi: [10.3847/1538-4357/aafb77](#)
- Baloković, M., Brightman, M., Harrison, F. A., et al. 2018, *The Astrophysical Journal*, 854, 42, [http://stacks.iop.org/0004-637X/854/i=1/a=42](#)
- Barthelmy, S. D., Barbier, L. M., Cummings, J. R., et al. 2005, *SSRv*, 120, 143, doi: [10.1007/s11214-005-5096-3](#)
- Basu-Zych, A. R., Lehmer, B. D., Hornschemeier, A. E., et al. 2013, *ApJ*, 762, 45, doi: [10.1088/0004-637X/762/1/45](#)
- Bellm, E. C., Kulkarni, S. R., Graham, M. J., et al. 2019, *PASP*, 131, 018002, doi: [10.1088/1538-3873/aaecbe](#)
- Benitez, N., Dupke, R., Moles, M., et al. 2014, arXiv e-prints, arXiv:1403.5237, doi: [10.48550/arXiv.1403.5237](#)
- Bertin, E., & Arnouts, S. 1996, *A&AS*, 117, 393, doi: [10.1051/aas:1996164](#)
- Boorman, P. G., Torres-Albà, N., Annun, A., et al. 2023, arXiv e-prints, arXiv:2311.04949, doi: [10.48550/arXiv.2311.04949](#)
- Brunner, H., Cappelluti, N., Hasinger, G., et al. 2008, *A&A*, 479, 283, doi: [10.1051/0004-6361:20077687](#)
- Brusa, M., Zamorani, G., Comastri, A., et al. 2007, *The Astrophysical Journal Supplement Series*, 172, 353, doi: [10.1086/516575](#)
- Burlon, D., Ajello, M., Greiner, J., et al. 2011, *The Astrophysical Journal*, 728, 58, [http://stacks.iop.org/0004-637X/728/i=1/a=58](#)
- Cappelluti, N., Hasinger, G., Brusa, M., et al. 2007, *The Astrophysical Journal Supplement Series*, 172, 341, doi: [10.1086/516586](#)
- Cappelluti, N., Brusa, M., Hasinger, G., et al. 2009, *A&A*, 497, 635, doi: [10.1051/0004-6361/200810794](#)
- Civano, F., Comastri, A., & Brusa, M. 2005, *Monthly Notices of the Royal Astronomical Society*, 358, 693, doi: [10.1111/j.1365-2966.2005.08821.x](#)
- Civano, F., Elvis, M., Brusa, M., et al. 2012, *ApJS*, 201, 30, doi: [10.1088/0067-0049/201/2/30](#)
- Civano, F., Hickox, R. C., Puccetti, S., et al. 2015, *The Astrophysical Journal*, 808, 185, doi: [10.1088/0004-637x/808/2/185](#)
- Civano, F., Zhao, X., Boorman, P., et al. 2023, arXiv e-prints, arXiv:2311.04832, doi: [10.48550/arXiv.2311.04832](#)

- Fabricant, D., Fata, R., Roll, J., et al. 2005, *PASP*, 117, 1411, doi: [10.1086/497385](https://doi.org/10.1086/497385)
- Fabricant, D., Fata, R., Epps, H., et al. 2019, *PASP*, 131, 075004, doi: [10.1088/1538-3873/ab1d78](https://doi.org/10.1088/1538-3873/ab1d78)
- Fiore, F., Brusa, M., Cocchia, F., et al. 2003, *A&A*, 409, 79, doi: [10.1051/0004-6361:20031031](https://doi.org/10.1051/0004-6361:20031031)
- Fruscione, A., McDowell, J. C., Allen, G. E., et al. 2006, in *Society of Photo-Optical Instrumentation Engineers (SPIE) Conference Series*, Vol. 6270, Society of Photo-Optical Instrumentation Engineers (SPIE) Conference Series, ed. D. R. Silva & R. E. Doxsey, 62701V, doi: [10.1117/12.671760](https://doi.org/10.1117/12.671760)
- Gaia Collaboration, Prusti, T., de Bruijne, J. H. J., et al. 2016, *A&A*, 595, A1, doi: [10.1051/0004-6361/201629272](https://doi.org/10.1051/0004-6361/201629272)
- Gaia Collaboration, Brown, A. G. A., Vallenari, A., et al. 2021, *A&A*, 649, A1, doi: [10.1051/0004-6361/202039657](https://doi.org/10.1051/0004-6361/202039657)
- Gardner, J. P., Mather, J. C., Clampin, M., et al. 2006, *SSRv*, 123, 485, doi: [10.1007/s11214-006-8315-7](https://doi.org/10.1007/s11214-006-8315-7)
- Gardner, J. P., Mather, J. C., Abbott, R., et al. 2023, *PASP*, 135, 068001, doi: [10.1088/1538-3873/acd1b5](https://doi.org/10.1088/1538-3873/acd1b5)
- Gehrels, N. 1986, *ApJ*, 303, 336, doi: [10.1086/164079](https://doi.org/10.1086/164079)
- Gehrels, N., Chincarini, G., Giommi, P., et al. 2004, *ApJ*, 611, 1005, doi: [10.1086/422091](https://doi.org/10.1086/422091)
- Gilli, R., Comastri, A., & Hasinger, G. 2007, *A&A*, 463, 79, doi: [10.1051/0004-6361:20066334](https://doi.org/10.1051/0004-6361:20066334)
- Harrison, F. A., Craig, W. W., Christensen, F. E., et al. 2013, *The Astrophysical Journal*, 770, 103, <http://stacks.iop.org/0004-637X/770/i=2/a=103>
- Harrison, F. A., Aird, J., Civano, F., et al. 2016, *The Astrophysical Journal*, 831, 185, <http://stacks.iop.org/0004-637X/831/i=2/a=185>
- Hernán-Caballero, A., Willmer, C. N. A., Varela, J., et al. 2023, *A&A*, 671, A71, doi: [10.1051/0004-6361/202244759](https://doi.org/10.1051/0004-6361/202244759)
- HI4PI Collaboration, Ben Bekhti, N., Flöer, L., et al. 2016, *A&A*, 594, A116, doi: [10.1051/0004-6361/201629178](https://doi.org/10.1051/0004-6361/201629178)
- Hornschemeier, A. E., Brandt, W. N., Garmire, G. P., et al. 2001, *The Astrophysical Journal*, 554, 742, doi: [10.1086/321420](https://doi.org/10.1086/321420)
- Hyun, M., Im, M., Smail, I. R., et al. 2023, *ApJS*, 264, 19, doi: [10.3847/1538-4365/ac9bf4](https://doi.org/10.3847/1538-4365/ac9bf4)
- Jansen, R. A., & Windhorst, R. A. 2018, *Publications of the Astronomical Society of the Pacific*, 130, 124001, doi: [10.1088/1538-3873/aae476](https://doi.org/10.1088/1538-3873/aae476)
- Kauffmann, G., Heckman, T. M., Tremonti, C., et al. 2003, *MNRAS*, 346, 1055, doi: [10.1111/j.1365-2966.2003.07154.x](https://doi.org/10.1111/j.1365-2966.2003.07154.x)
- Kewley, L. J., Dopita, M. A., Sutherland, R. S., Heisler, C. A., & Trevena, J. 2001, *ApJ*, 556, 121, doi: [10.1086/321545](https://doi.org/10.1086/321545)
- Laird, E. S., Nandra, K., Georgakakis, A., et al. 2008, *The Astrophysical Journal Supplement Series*, 180, 102, doi: [10.1088/0067-0049/180/1/102](https://doi.org/10.1088/0067-0049/180/1/102)
- LaMassa, S. M., Urry, C. M., Cappelluti, N., et al. 2016, *The Astrophysical Journal*, 817, 172, doi: [10.3847/0004-637x/817/2/172](https://doi.org/10.3847/0004-637x/817/2/172)
- Lansbury, G. B., Stern, D., Aird, J., et al. 2017, *The Astrophysical Journal*, 836, 99, doi: [10.3847/1538-4357/836/1/99](https://doi.org/10.3847/1538-4357/836/1/99)
- Luo, B., Brandt, W. N., Xue, Y. Q., et al. 2017, *ApJS*, 228, 2, doi: [10.3847/1538-4365/228/1/2](https://doi.org/10.3847/1538-4365/228/1/2)
- Maccacaro, T., Gioia, I. M., Wolter, A., Zamorani, G., & Stocke, J. T. 1988, *ApJ*, 326, 680, doi: [10.1086/166127](https://doi.org/10.1086/166127)
- Madsen, K., Hickox, R., Bachetti, M., et al. 2019, in *Bulletin of the American Astronomical Society*, Vol. 51, 166
- Mainzer, A., Bauer, J., Cutri, R. M., et al. 2014, *ApJ*, 792, 30, doi: [10.1088/0004-637X/792/1/30](https://doi.org/10.1088/0004-637X/792/1/30)
- Marchesi, S., Civano, F., Elvis, M., et al. 2016, *The Astrophysical Journal*, 817, 34, doi: [10.3847/0004-637x/817/1/34](https://doi.org/10.3847/0004-637x/817/1/34)
- Marchesi, S., Gilli, R., Lanzuisi, G., et al. 2020, *A&A*, 642, A184, doi: [10.1051/0004-6361/202038622](https://doi.org/10.1051/0004-6361/202038622)
- Masci, F. J., Laher, R. R., Rusholme, B., et al. 2019, *PASP*, 131, 018003, doi: [10.1088/1538-3873/aae8ac](https://doi.org/10.1088/1538-3873/aae8ac)
- Masini, A., Civano, F., Comastri, A., et al. 2018a, *The Astrophysical Journal Supplement Series*, 235, 17, doi: [10.3847/1538-4365/aaa83d](https://doi.org/10.3847/1538-4365/aaa83d)
- Masini, A., Comastri, A., Civano, F., et al. 2018b, *The Astrophysical Journal*, 867, 162, doi: [10.3847/1538-4357/aae539](https://doi.org/10.3847/1538-4357/aae539)
- McLeod, B., Fabricant, D., Nyström, G., et al. 2012, *PASP*, 124, 1318, doi: [10.1086/669044](https://doi.org/10.1086/669044)
- Mink, D. J., Wyatt, W. F., Caldwell, N., et al. 2007, in *Astronomical Society of the Pacific Conference Series*, Vol. 376, *Astronomical Data Analysis Software and Systems XVI*, ed. R. A. Shaw, F. Hill, & D. J. Bell, 249
- Mullaney, J. R., Del-Moro, A., Aird, J., et al. 2015, *ApJ*, 808, 184, doi: [10.1088/0004-637X/808/2/184](https://doi.org/10.1088/0004-637X/808/2/184)
- Ni, Q., Brandt, W. N., Chen, C.-T., et al. 2021, *The Astrophysical Journal Supplement Series*, 256, 21, doi: [10.3847/1538-4365/ac0dc6](https://doi.org/10.3847/1538-4365/ac0dc6)
- Nowak, M. 2016. https://cxc.cfa.harvard.edu/csc/memos/files/Nowak_csc2_variability_and_color.pdf
- O'Brien, R., Jansen, R. A., Grogin, N. A., et al. 2024, *arXiv e-prints*, arXiv:2401.04944, doi: [10.48550/arXiv.2401.04944](https://doi.org/10.48550/arXiv.2401.04944)
- Oh, K., Koss, M., Markwardt, C. B., et al. 2018, *The Astrophysical Journal Supplement Series*, 235, 4, doi: [10.3847/1538-4365/aaa7fd](https://doi.org/10.3847/1538-4365/aaa7fd)

- Park, T., Kashyap, V. L., Siemiginowska, A., et al. 2006, *The Astrophysical Journal*, 652, 610, doi: [10.1086/507406](https://doi.org/10.1086/507406)
- Pineau, F.-X., Derriere, S., Motch, C., et al. 2017, *A&A*, 597, A89, doi: [10.1051/0004-6361/201629219](https://doi.org/10.1051/0004-6361/201629219)
- Primini, F. A., & Kashyap, V. L. 2014, *ApJ*, 796, 24, doi: [10.1088/0004-637X/796/1/24](https://doi.org/10.1088/0004-637X/796/1/24)
- Puccetti, S., Vignali, C., Cappelluti, N., et al. 2009, *The Astrophysical Journal Supplement Series*, 185, 586, doi: [10.1088/0067-0049/185/2/586](https://doi.org/10.1088/0067-0049/185/2/586)
- Ranalli, P., Comastri, A., & Setti, G. 2005, *A&A*, 440, 23, doi: [10.1051/0004-6361:20042598](https://doi.org/10.1051/0004-6361:20042598)
- Ricci, C., Ueda, Y., Koss, M. J., et al. 2015, *The Astrophysical Journal Letters*, 815, L13. <http://stacks.iop.org/2041-8205/815/i=1/a=L13>
- Ricci, C., Trakhtenbrot, B., Koss, M. J., et al. 2017, *The Astrophysical Journal Supplement Series*, 233, 17. <http://stacks.iop.org/0067-0049/233/i=2/a=17>
- Schlaflly, E. F., Meisner, A. M., & Green, G. M. 2019, *ApJS*, 240, 30, doi: [10.3847/1538-4365/aafbea](https://doi.org/10.3847/1538-4365/aafbea)
- Schmidt, M., Hasinger, G., Gunn, J., et al. 1998, *A&A*, 329, 495. <https://arxiv.org/abs/astro-ph/9709144>
- Smolčić, V., Delvecchio, I., Zamorani, G., et al. 2017, *A&A*, 602, A2, doi: [10.1051/0004-6361/201630223](https://doi.org/10.1051/0004-6361/201630223)
- Stocke, J. T., Morris, S. L., Gioia, I. M., et al. 1991, *ApJS*, 76, 813, doi: [10.1086/191582](https://doi.org/10.1086/191582)
- Sutherland, W., & Saunders, W. 1992, *MNRAS*, 259, 413, doi: [10.1093/mnras/259.3.413](https://doi.org/10.1093/mnras/259.3.413)
- Taylor, A. J., Barger, A. J., Cowie, L. L., et al. 2023, arXiv e-prints, arXiv:2302.11581, doi: [10.48550/arXiv.2302.11581](https://doi.org/10.48550/arXiv.2302.11581)
- Torres-Albà, N., Marchesi, S., Zhao, X., et al. 2021, arXiv e-prints, arXiv:2109.00599. <https://arxiv.org/abs/2109.00599>
- Treister, E., Urry, C. M., & Virani, S. 2009, *The Astrophysical Journal*, 696, 110. <http://stacks.iop.org/0004-637X/696/i=1/a=110>
- Ueda, Y., Akiyama, M., Hasinger, G., Miyaji, T., & Watson, M. G. 2014, *The Astrophysical Journal*, 786, 104. <http://stacks.iop.org/0004-637X/786/i=2/a=104>
- Wang, S.-G., Su, D.-Q., Chu, Y.-Q., Cui, X., & Wang, Y.-N. 1996, *ApOpt*, 35, 5155, doi: [10.1364/AO.35.005155](https://doi.org/10.1364/AO.35.005155)
- Wik, D. R., Hornstrup, A., Molendi, S., et al. 2014, *The Astrophysical Journal*, 792, 48, doi: [10.1088/0004-637x/792/1/48](https://doi.org/10.1088/0004-637x/792/1/48)
- Willmer, C. N. A., Ly, C., Kikuta, S., et al. 2023, *ApJS*, 269, 21, doi: [10.3847/1538-4365/acf57d](https://doi.org/10.3847/1538-4365/acf57d)
- Willner, S. P., Gim, H. B., Polletta, M. d. C., et al. 2023, arXiv e-prints, arXiv:2309.13008, doi: [10.48550/arXiv.2309.13008](https://doi.org/10.48550/arXiv.2309.13008)
- Windhorst, R. A., Cohen, S. H., Jansen, R. A., et al. 2023, *AJ*, 165, 13, doi: [10.3847/1538-3881/aca163](https://doi.org/10.3847/1538-3881/aca163)
- Wright, E. L., Eisenhardt, P. R. M., Mainzer, A. K., et al. 2010, *The Astronomical Journal*, 140, 1868. <http://stacks.iop.org/1538-3881/140/i=6/a=1868>
- Xue, Y. Q., Luo, B., Brandt, W. N., et al. 2011, *The Astrophysical Journal Supplement Series*, 195, 10, doi: [10.1088/0067-0049/195/1/10](https://doi.org/10.1088/0067-0049/195/1/10)
- Yang, G., Brandt, W. N., Luo, B., et al. 2016, *The Astrophysical Journal*, 831, 145, doi: [10.3847/0004-637x/831/2/145](https://doi.org/10.3847/0004-637x/831/2/145)
- Yuan, H., Zhang, H., Zhang, Y., et al. 2013, *Astronomy and Computing*, 3, 65, doi: [10.1016/j.ascom.2013.12.001](https://doi.org/10.1016/j.ascom.2013.12.001)
- Zhao, X., Marchesi, S., Ajello, M., et al. 2021b, *A&A*, 650, A57, doi: [10.1051/0004-6361/202140297](https://doi.org/10.1051/0004-6361/202140297)
- Zhao, X., Civano, F., Fornasini, F. M., et al. 2021a, *Monthly Notices of the Royal Astronomical Society*, 508, 5176, doi: [10.1093/mnras/stab2885](https://doi.org/10.1093/mnras/stab2885)

APPENDIX

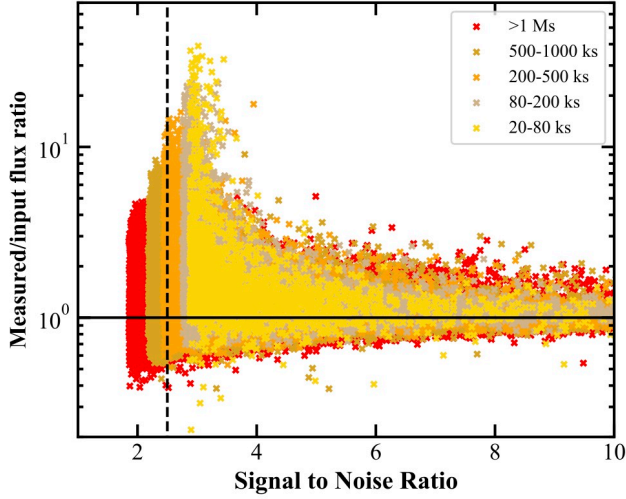


Figure 24. Ratio of measured (3–24 keV) flux to true flux as a function of measured signal to noise ratio. Points show the ratio for simulated (Section 3) individual sources with different exposure times indicated as shown in the legend. Points include only (simulated) sources detected with $>95\%$ reliability. The vertical dashed line indicates $S/N = 2.5$, which was the cut for calculating $\log N - \log S$ (Section 7.1).

APPENDIX A. MEASURED TO INPUT FLUX AND SIGNAL TO NOISE RATIO

The accuracy of the NuSTAR source flux measurement is strongly correlated with the S/N (as defined in Section 7.1). Figure 24 shows the simulation results. The dispersion of the measured to input flux ratio is quite high at low S/N, and there is a strong bias for measured fluxes to be higher than the true flux, especially at low S/N.

APPENDIX B. NUSTAR AND XMM-NEWTON CATALOG DESCRIPTION

The description of each column of the 95% reliability level catalog of NuSTAR detected sources in cycle 6 and cycles 5+6 survey is in Table 9. The description of each column of the catalog of XMM-Newton detected sources is in Table 10.

In future work, the NuSTAR sources can be referred to as “NuSTAR JHHMMSS+DDMM.m” where the sequence (JHHMMSS+DDMM.m) is the contents of column 2 of either of the NuSTAR data tables. Similarly, the XMM sources can be referred to as “TDFXMM JHHMMSS+DDMM.m” with the sequence given in column 2 of the XMM-Newton data table.

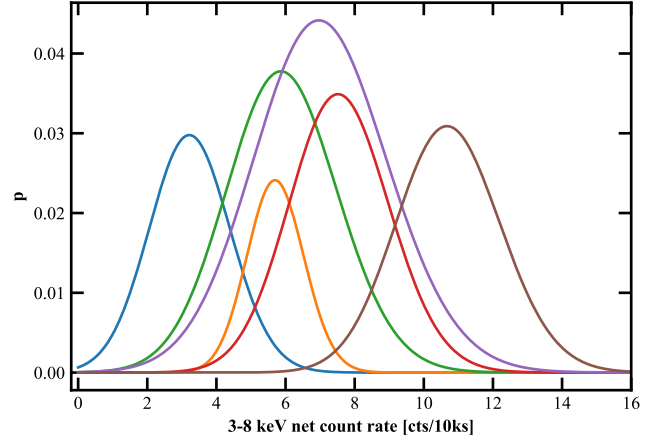


Figure 25. 3–8 keV net count-rate posterior probability distribution of NuSTAR source ID 58 in each epoch. Epochs are distinguished by color in the order blue, orange, green, red, violet, brown, magenta (the same as Figure 27, which shows dates for each epoch). Count-rate PPDs are count PPDs divided by exposure time.

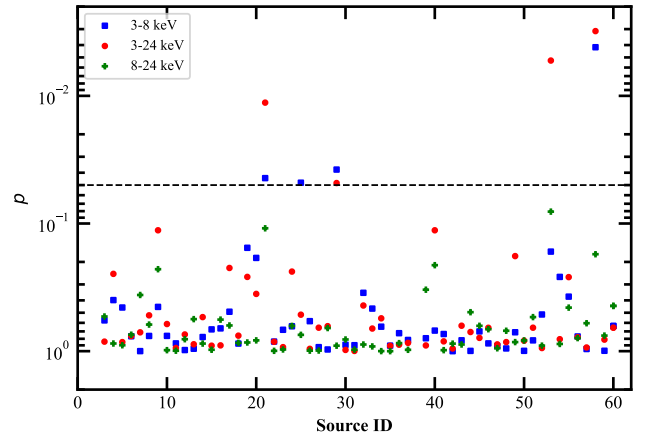


Figure 26. “False-alarm” probability p of each source. Colors and point shapes show different energy bands as indicated in the legend. The horizontal dashed line shows $p = 0.05 \approx 2\sigma$. Points above this line have higher probability of being true variables.

APPENDIX C. HECTOSPEC OBSERVATIONS OF NON-XMM TARGETS IN NEP-TDF

Table 11 reports the coordinates, redshifts, and spectral types of the 40 VLA and Chandra sources in the NEP-TDF.

APPENDIX D. VARIABILITY CALCULATION

Studying source variability is the prime goal of the NuSTAR NEP-TDF. Thanks to the multi-year and multi-epoch observations in the field, NEP-TDF became the first NuSTAR contiguous survey to study hard-X-ray (3–24 keV) variability.

The traditional method for analyzing X-ray-source variability (e.g., [Yang et al. 2016](#)) is not suitable for NuSTAR contiguous surveys because that method requires good counting statistics and negligible backgrounds. After adding all seven epochs in cycles 5 and 6, the median NuSTAR-detected (3–24 keV) source has 120 net source counts on top of 700 background counts. This gives low S/N and an uncertain net count rate for individual epochs. Therefore, we developed a dedicated pipeline to analyze source variability in the low-count regime. This paper describes the pipeline and briefly summarizes the source variability results. A future paper will provide a systematic discussion of source variability in the NuSTAR and XMM-Newton NEP-TDF.

The pipeline follows the Bayesian approach developed by [Primini & Kashyap \(2014\)](#) and used to generate the Chandra Source Catalog¹⁵ (CSC). The key calculation is the probability distribution of the expected net source counts in each epoch. This approach is able to deal with the Poisson (not Gaussian) statistical noise and is valid in low-counts regimes because it uses Poisson likelihoods. The net count posterior probability distribution (PPD) was calculated using Equation 16 of [Primini & Kashyap \(2014\)](#) assuming non-informative prior distributions. We used a circle with 20'' radius to extract the total and background counts from each epoch's image and background map. Thus we analyzed only the inter-epoch variability rather than the intra-epoch's variability. As the sources are not detectable in every epoch, we used a fixed source position (the one reported in the catalog) for all epochs and energy bands. Figure 25 shows the net count-rate PPDs for the most-likely variable source (ID 58).

The probability of source variability came from applying the χ^2 test following the CSC method ([Nowak 2016](#)). The method computes the deviation between the most probable flux in each epoch and the most probable flux in the entire survey. The null hypothesis is that there is no variability, and the “false-alarm” probability p was calculated from equation 10 of [Nowak \(2016\)](#). A smaller p suggests a larger probability that variability exists. Figure 26 shows p for the NuSTAR sources. Of the 60 sources, 44 were observed in all seven

epochs, and 9, 4, and 3 sources were observed in six, five, and one epoch(s), respectively. Four sources (ID 21/25/29/58) show variability at $p < 0.05 (\sim 2\sigma)$ in at least one band, and Figure 27 shows their light curves. The same pipeline can be used for XMM-Newton data, and those results will be presented in a future paper.

¹⁵ <https://cxc.cfa.harvard.edu/csc/>

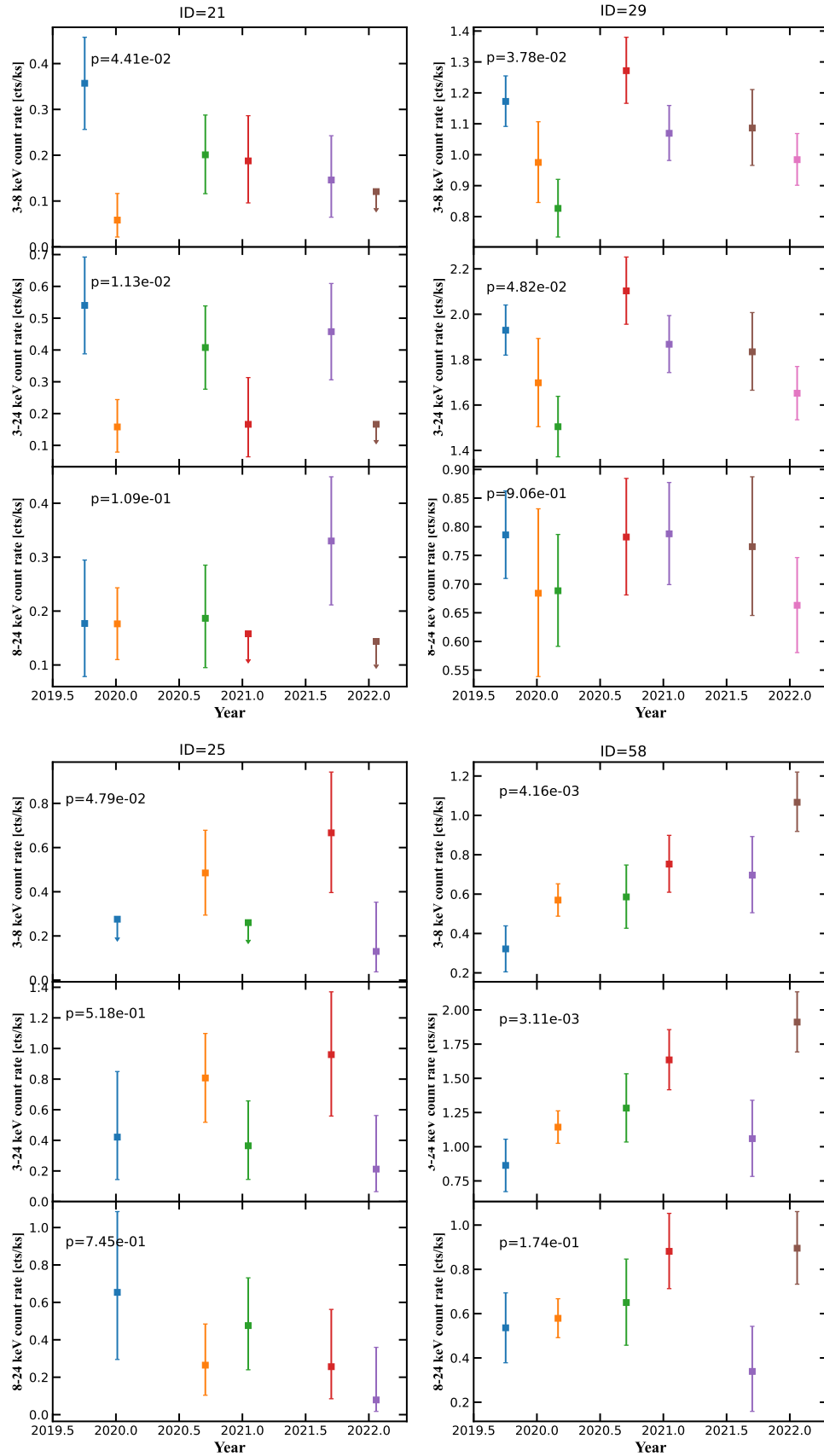


Figure 27. Light curves of the four sources that show the most variability. Sources are labeled at the top of each panel, and sections top to bottom show different energy ranges as labeled. Point colors for each epoch are the same as in Figure 25.

Table 9. NuSTAR 95% reliability source catalog description.

Col.	Description
1	NuSTAR source ID used in this paper.
2	Source name (use “NuSTAR JHHMMSS+DDMM.m”).
3–4	X-ray coordinates (J2000) of the source in whichever energy band has the highest DET_ML.
5	3–24 keV band deblended DET_ML (–99 if the source is not detected in a given band).
6	3–24 keV band vignetting-corrected exposure time in ks at the position of the source.
7	3–24 keV band total counts (source + background) in a 20'' radius aperture.
8	3–24 keV band deblended background counts in a 20'' radius aperture (–99 if the source is not detected in a given band).
9	3–24 keV band not deblended background counts in a 20'' radius aperture.
10	3–24 keV band net counts (deblended if detected & above DET_ML threshold or 90% confidence upper limit if undetected or detected but below DET_ML threshold) in a 20'' radius aperture.
11–12	3–24 keV band 1σ positive/negative net counts uncertainty (–99 for upper limits).
13	3–24 keV band count rate (90% confidence upper limit if not detected or detected but below the threshold) in a 20'' radius aperture.
14	3–24 keV band aperture corrected flux ($\text{erg cm}^{-2} \text{s}^{-1}$; 90% confidence upper limit if below 95% confidence threshold).
15–16	3–24 keV band positive/negative flux uncertainties ($\text{erg cm}^{-2} \text{s}^{-1}$; –99 for upper limits).
17–28	same as columns 5–16 but for 3–8 keV.
29–40	same as columns 5–16 but for 8–24 keV.
41–52	same as columns 5–16 but for 8–16 keV.
53–64	same as columns 5–16 but for 16–24 keV.
65	Hardness ratio computed using BEHR.
66–67	Upper/lower limit of hardness ratio.
68	XMM-Newton source ID from the XMM-Newton catalog (–1 if non-detection).
69,70	Soft X-ray coordinates of the associated source (–1 if no XMM-Newton counterpart).
71	NuSTAR to soft X-ray counterpart position separation in arcsec.
72	3–8 keV flux converted from XMM-Newton 2–10 keV flux (90% confidence upper limit if $\text{mlmin} < 6$).
73	3–8 keV XMM-Newton flux 1σ uncertainty (–99 for upper limit).
74	Flag for NuSTAR counterparts (S, P, Sec, C if the XMM source is the single, primary, secondary, or confusing counterpart of the NuSTAR source, respectively).
75	Flag for ancillary class (S for secure, A for ambiguous, and U for unidentified)
76,77	Ancillary coordinates of the associated source (–99 if no detection).
78	Optical (HSC) <i>i</i> band AB magnitude (–99 if no detection).
79,80	MMIRS <i>J</i> and <i>K</i> band AB magnitude (–99 if no detection).
81,82	WISE <i>W1</i> and <i>W2</i> band AB magnitude (–99 if no detection).
83	VLA 3 GHz counterpart ID from Hyun et al. (2023) .
84	VLA 3 GHz flux density in μJy (Hyun et al. 2023).
85	HST F606W AB magnitude (–99 if no detection).
86	JWST F444W AB magnitude (–99 if no detection).
87	Spectroscopic redshift of the associated source.
88	Photometric redshift of the associated source.
89	Spectroscopic classification (Q for quasars, G for galaxies, S for stars, N/A if no measurement). Galaxies are defined as objects without broad emission lines and therefore include type 2 AGN.
90	Luminosity distance in Mpc (70/0.3/0.7 cosmology, –99 if no redshift measurement).
91	10–40 keV band rest-frame luminosity (–99 if no redshift measurement).
92–93	10–40 keV band 1σ positive/negative rest-frame luminosity uncertainty (–99 if no redshift measurement).
94	Source ID in the Zhao et al. (2021a) NuSTAR cycle 5 catalog (–99 for non-detection in the cycle 5 catalog).

Table 10. XMM-Newton source catalog description.

Col.	Description
1	XMM-Newton source ID used in this paper.
2	XMM-Newton source name (use “TDFXMM JHHMMSS+DDMM.m”).
3–4	X-ray coordinates (J2000) of the source.
5	0.5–2 keV band DET_ML.
6	0.5–2 keV band vignetting-corrected exposure time (in ks) at the position of the source.
7	0.5–2 keV band net counts of the source (90% confidence upper limit if <code>mlmin</code> < 6).
8	0.5–2 keV band net counts 1σ uncertainty (–99 for upper limits).
9	0.5–2 keV band flux ($\text{erg cm}^{-2} \text{s}^{-1}$; 90% confidence upper limit if <code>mlmin</code> < 6).
10	0.5–2 keV band flux 1σ error (–99 for upper limits).
11–16	same as columns 5–10 but for 2–10 keV.
17	Hardness ratio (90% confidence upper or lower limits if not constrained).
18	Hardness ratio 1σ uncertainty (–99 for upper limits and 99 for lower limits).
19	NuSTAR source ID from the NuSTAR cycles 5+6 catalog (–1 if non-detection).
20	Flag for NuSTAR cycle 56 counterparts (S, P, Sec, C if the XMM source is the single, primary, secondary, or confused counterpart of the NuSTAR source, respectively).
21	NuSTAR source ID from the NuSTAR cycle 6 catalog (–1 if non-detection).
22	Flag for NuSTAR cycle 6 counterparts (S, P, Sec, C if the XMM source is the single, primary, secondary, or confused counterpart of the NuSTAR source, respectively).
23	Flag for ancillary class (S for secure, A for ambiguous, or U for unidentified)
24,25	Ancillary coordinates of the associated source (–99 if no detection).
26	Optical (HSC) <i>i</i> band AB magnitude (–99 if no detection).
27	Flag for SDSS detection (1 if SDSS has detection, –1 if SDSS has no detection)
28	Flag for J-PAS detection (1 if J-PAS has detection, –1 if J-PAS has no detection)
29,30	MMIRS <i>J</i> and <i>K</i> band AB magnitude (–99 if no detection).
31,32	WISE <i>W1</i> and <i>W2</i> band AB magnitude (–99 if no detection).
33	VLA 3 GHz counterpart ID from Hyun et al. (2023) .
34	VLA 3 GHz flux in μJy (Hyun et al. 2023).
35	HST F606W AB magnitude (–99 if no detection).
36	JWST F444W AB magnitude (–99 if no detection).
37	Spectroscopic redshift of the associated source (–99 if no measurement).
38	Photometric redshift of the associated source (–99 if no redshift measurement).
39	Spectroscopic classification (Q for quasars, G for galaxies, S for stars, N/A if no measurement). Galaxies are defined as objects without broad emission lines and therefore include type 2 AGN.
41	0.5–2 keV band rest-frame luminosity before correcting for absorption assuming a photon index of $\Gamma = 1.40$ (–99 if not detected in the 0.5–2 keV band).
42	0.5–2 keV band rest-frame luminosity 1σ uncertainty.
43	2–10 keV band rest-frame luminosity before correcting for absorption assuming a photon index of $\Gamma = 1.80$ (–99 if not detected in the 2–10 keV band).
44	2–10 keV band rest-frame luminosity 1σ uncertainty.

Table 11. Hectospec observations of 40 VLA and Chandra targets in NEP-TDF.

Name	RA	DEC	z	Class
VLA 3	260.351313	65.814148	0.2923	G
VLA 48	260.507012	65.740059	0.6297	G
VLA 52	260.522058	65.680923	0.5010	G
VLA 62	260.530900	65.924820	0.2720	G
VLA 74	260.562717	65.810898	0.0806	G
VLA 82	260.573729	65.660584	0.6312	G
VLA 140	260.638762	65.653336	0.1785	G
VLA 159	260.648546	65.797379	0.2953	G
VLA 164	260.652038	65.931777	0.0415	G
VLA 173	260.658704	65.849815	0.4972	G
VLA 185	260.666254	65.671364	2.80	Q ^a
VLA 198	260.674983	65.976944	0.0746	G
VLA 200	260.678471	65.83725	0.5658	G
VLA 222	260.692892	65.861908	0.2946	G
VLA 246	260.71455	65.753357	0.5397	G
VLA 260	260.721475	65.813164	0.545	G
VLA 382	260.799721	65.837288	0.3759	G
VLA 386	260.805617	65.730148	1.0415	G
VLA 429	260.838487	65.837677	0.8905	G
VLA 439	260.846929	65.744003	0.3774	G
VLA 477	260.881892	65.722382	0.3748	G
VLA 514	260.910617	65.905113	0.3579	G
VLA 528	260.919458	65.831345	0.3762	G
VLA 561	260.946979	65.874069	0.3820	G
VLA 574	260.961083	65.761307	0.0964	G
VLA 592	260.978937	65.782906	0.2923	G
VLA 628	261.009637	65.638786	0.5643	G
VLA 656	261.038017	65.746704	0.5567	G
VLA 675	261.057729	65.784676	0.2946	G
VLA 688	261.073267	65.855888	0.1055	G
VLA 705	261.116296	65.777801	0.4136	G
VLA 721	261.151712	65.851639	0.4464	G
VLA 752	261.251333	65.815597	0.5010	G
VLA 755	261.289646	65.827973	0.1816	G
Cha 11	260.729742	65.926109	0.008	G
Cha 38	260.404500	65.799156	0	S
Cha 43	260.538454	65.827545	0.776	G
Cha 47	260.397692	65.838997	0.6487	G
Cha 50	260.804071	65.886581	0.8347	Q
Cha 76	260.363158	65.852623	0.2762	G

NOTE—The source name is composed of catalog (VLA; [Hyun et al. 2023](#)) or Chandra (P. Maksym et al., in prep.) and the ID of the source in the corresponding catalog. G, Q, and S in spectral class represent galaxy, quasar, and star, respectively. Narrow emission-line (type 2) quasars are categorized as galaxies.

^aThis broad absorption-line quasar also has a JCMT detection.